Challenging the Limit of Strengthening by γ/γ' Lattice Misfit on the High Temperature Creep Properties of Ni-Base Single Crystal Superalloy

SATOSHI UTADA, TADAHARU YOKOKAWA, TOSHIHARU KOBAYASHI,
MICHINARI YUYAMA, HIROSHI HARADA, TOSHIO OSADA,
and KYOKO KAWAGISHI

TMS-238MoIr previously achieved a record creep rupture life of 4044 hours at 1100 °C/137 MPa—more than twice that of the sixth-generation Ni-base single crystal superalloy TMS-238—corresponding to a temperature capability of 1136 °C (Larson–Millar conversion by 1000 hours rupture life under 137 MPa). This alloy was designed to enhance the high-temperature low-stress creep performance of TMS-238 by adding 1.5 at. pct Mo and 2 at. pct Ir. This study investigates the mechanisms behind this exceptional high-temperature creep performance and its limitations at other conditions by comparing it to a counterpart alloy, TMS-238MoRu (TMS-238 + 1.5 at. pct Mo and 2 at. pct Ru). At 1100 °C/137 MPa, TMS-238MoIr's superior life was attributed to the combined effects of a refined γ/γ' interfacial dislocation network achieved through increased magnitude of lattice misfit by Mo addition, and the suppression of topologically close-packed (TCP) phases by Ir. In contrast, TMS-238MoRu failed in only 870 hours due to extensive TCP precipitation. The high γ/γ' coherency stress and decreased stacking fault energy in both modified alloys induced stacking faults in the γ matrix during the initial heat treatment, before the creep test. These pre-existing faults served as potent nucleation sites for TCP phases at temperatures below 900 °C. Consequently, TCP precipitate-assisted deformation significantly reduced the creep lives of both concept alloys at 900 °C/392 MPa. These findings demonstrate that lattice misfit tuning must be carefully balanced with stacking fault energy and γ/γ' phase stability to optimize creep performance across a wide range of temperatures in advanced Ni-base superalloys.

https://doi.org/10.1007/s11661-025-08089-5

I. INTRODUCTION

THE creep properties of a Ni-base single crystal (SC) superalloy for gas turbine application are important factors determining component life of turbine blades and the thermal efficiency of the gas turbine systems.[1–3] To enhance the performance of the aero engines, the temperature capability of Ni-base SC superalloy has been improved primarily by modification of their chemical compositions.[1,4] Up to now, from the information available in literature, third-generation SC superalloys containing 4–6 wt pct Re are widely used in commercial applications.[5–8] Recent trends in the alloy development field aim at more economical alloys with low or zero Re content, as Re is often considered as expensive and strategic material.[8–12] These low Re alloys attempt to balance the cost and high-temperature properties; however, they do not always possess high-temperature properties comparable to the high-performance alloys such as sixth-generation SC superalloy TMS-238 and its advanced version, TMS-238MoIr (TMS-238 + 1.5 at. pct Mo + 2 at. pct Ir), developed through the NIMS-ADP (alloy design program) approach.[13–17]

Despite the general trend against expensive materials, there is still a need to improve the high-temperature capabilities of the materials, not only considering the thermal efficiency of the gas turbine systems, but also for specific operational conditions of aero engines. These

---

Toshiharu Kobayashi: Deceased author.

SATOSHI UTADA, TADAHARU YOKOKAWA, TOSHIHARU KOBAYASHI, MICHINARI YUYAMA, HIROSHI HARADA, TOSHIO OSADA, and KYOKO KAWAGISHI are with the Research Center for Structural Materials, National Institute for Materials Science, 1-2-1 Sengen, Tsukuba, Ibaraki, 305-0047, Japan. Contact email: UTADA.Satoshi@nims.go.jp

Manuscript submitted September 30, 2025; accepted December 11, 2025.

include, for example, application of SC superalloys for non-cooled low-pressure turbine blades,[18] smaller gas turbine for helicopter or private jets that uses very small blades without cooling systems, and one engine inoperative (OEI) events that require contingency power operation with overheating.[19–21] Therefore, studies on the creep properties of SC superalloys at temperatures above 1200 °C have become more active.[22–27] Moreover, for resource sustainability and stable supply purposes, refurbishment and recycling methods for turbine blades have been studied.[28–30] These methods should remove barriers for high-end materials to be applied to commercial components. In fact, a conceptual alloy with costly Pt addition has been designed and tested aiming at application at such high temperatures.[26,31,32]

Ni-base SC superalloys leverage several mechanisms to enhance high-temperature creep properties. The most fundamental one is to control the fraction of coherent γ' ($L1_2$) precipitates to 60–70 pct and their sizes to 300-400 nm to hinder dislocation glide.[33] Solid solution strengthening of FCC γ matrix by adding Re is well known as "rhenium effect," as this element has smaller diffusion coefficient than other alloying elements, thus slows down dislocation mobility and contributes to extend the creep life.[34,35] However, due to the limited solubility of Re in Ni-base superalloys, the precipitation of topologically closed packed (TCP) phases, which decrease creep durability of the material, can be an issue when the Re is over-alloyed.[36–39] To avoid TCP precipitation and improve γ/γ' phase stability, Ru, a platinum group metal (PGM), is added to develop fourth and fifth-generation Ni-base SC superalloys with significantly improved high-temperature creep strength.[40–45]

Another important parameter determining high-temperature low-stress creep durability is the magnitude of negative lattice misfit between γ matrix and γ' precipitates. Under high-temperature creep loads, cubic γ' precipitates in Ni-base SC superalloys typically transform into a plate-like structure known as γ'-raft, which develops transverse to the tensile loading direction.[46–49] When the negative lattice misfit is larger, the γ/γ' interfacial dislocation network of the γ/γ'-raft become finer, which then acts as obstacles for dislocation climb and γ' shearing during the creep deformation.[22,41,46,50–55] By effectively combining γ/γ'-misfit strengthening, solid solution strengthening (by W, Re, and Ta), and enhancing the microstructural stability by Ru addition, NIMS developed sixth-generation SC superalloy TMS-238 that exhibits excellent creep properties and environmental resistance across wide temperature ranges.[13,56] Using the Larson–Miller equation, the temperature capability of TMS-238 is estimated to be 1117 °C for a 1000-hour creep rupture life at 137 MPa.

Targeting at improving operating temperature capability of TMS-238 by further advancing γ/γ' misfit strengthening, TMS-238MoIr was developed by adding 1.5 at. pct Mo and 2 at. pct Ir to the base material TMS-238 in the previous study.[17,57] Mo was added on top of the original 0.7 at. pct content because it tends to partition into γ matrix and increases the magnitude of negative lattice misfit[50,58,59]; however, Mo also promotes precipitation of TCP phase.[58] Ir addition was intended to counter this TCP formation and improve γ/γ' phase stability.[17,50,57,60] The developed alloy TMS-238MoIr achieved the longest creep life of 4044 hours among all published SC superalloys at 1100 °C/137 MPa, a service temperature of 1136 °C using the same Larson-Miller conversion for 1000 hours life under 137 MPa load as summarized in Figure 1.[17]

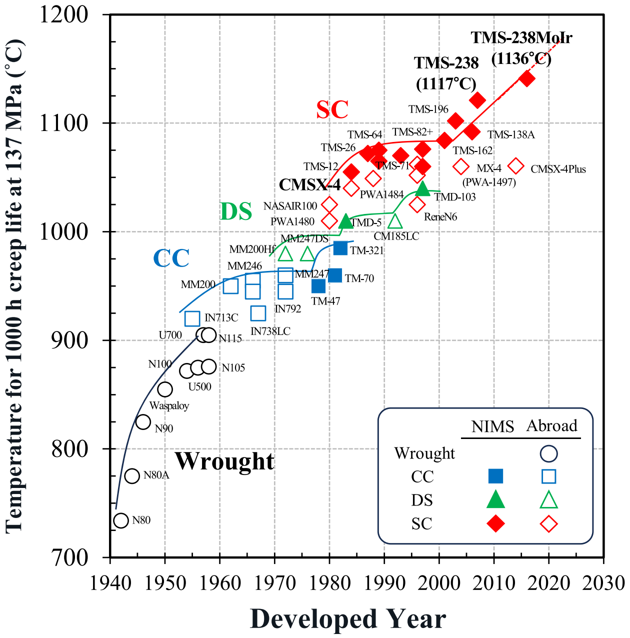

Fig. 1—Temperature capability of Ni-base superalloys for turbine blade applications, estimated using the Larson-Miller approach for a 1000 h creep life at 137 MPa.

The remaining tasks from the previous studies include a detailed analysis on the mechanism behind the exceptional creep life of TMS-238MoIr under high-temperature low-stress creep conditions, and an understanding of the γ/γ' phase stability and creep performances under other conditions. To confirm effect of Ir in this alloy system, we also prepared TMS-238MoRu (TMS-238 with 1.5 at. pct Mo and 2 at. pct Ru added) as a counterpart. The effects of these modifications on creep behaviors, lattice misfit, dislocation structure, and TCP phase stability were systematically investigated.

II. EXPERIMENTAL DETAILS

A. *Alloy Design Strategy and Single Crystal Sample Preparation*

Two modified TMS-238 variations, TMS-238MoRu and TMS-238MoIr, were prepared as listed in Table I. Al content was adjusted so that the estimated γ' volume fraction will be 59-61 pct at 1100 °C. The materials properties of the experimental alloys, such as γ/γ' lattice misfit (δ), solubility index (SI), and density, were estimated using the NIMS-ADP[14,15,57,61,62] and they are summarized in Table I. High SI values (SI > 1.2)

Table I. Chemical Composition and Estimated Properties of the Experimental Alloys

		Composition (Ni-Bal)										γ/γ' Lattice Misfit at 1100 °C (Pct)	SI	Density (g/cm^3)
		Co	Cr	Mo	W	Al	Ta	Hf	Re	Ir	Ru			
TMS-238	at. pct	7.0	5.6	0.7	1.4	13.9	2.7	0.04	2.2		3.1	− 0.34	1.25	8.99
	wt pct	6.5	4.6	1.1	4.0	5.9	7.6	0.1	6.4		5.0			
TMS-238MoRu	at. pct	7.0	5.6	2.2	1.4	13.1	2.7	0.04	2.2		5.1	− 0.50	1.50	9.09
	wt pct	6.4	4.5	3.2	3.9	5.45	7.4	0.1	6.2		8.0			
TMS-238MoIr	at. pct	7.0	5.6	2.2	1.4	13.1	2.7	0.04	2.2	2.0	3.1	− 0.41	1.48	9.36
	wt pct	6.2	4.4	3.1	3.8	5.3	7.2	0.1	6.1	5.8	4.8			

Table II. Heat Treatment Conditions Applied to the Experimental Materials

	Solution	1st Aging	2nd Aging
TMS-238	1345 °C, 20 h	1150 °C, 2 h	870 °C, 20 h
TMS-238MoRu	1340 °C, 20 h	1100 °C, 4 h	870 °C, 20 h
TMS-238MoIr	1340 °C, 20 h	1150 °C, 4 h	870 °C, 20 h

suggest an increased risk of TCP precipitation during high-temperature exposure,[15,63] although this does not account for γ/γ' stabilization effect by Ru or Ir. With a 2 at. pct Ru addition, this SI limit increases from 1.2 to 1.3, meaning that the composition of the baseline TMS-238 is within an acceptable range.[63] According to the estimation, additional Mo can be very efficient in increasing the magnitude of negative γ/γ' lattice misfit. However, simultaneously, increased SI values give a warning that there is very high chance of early TCP nucleation.

The single crystal materials were fabricated from high-purity raw materials using the withdrawing precision casting method in a directional solidification vacuum induction melting furnace with a withdrawal rate of 200 mm/h. The cast bars have a 10.5 mm diameter and a 130 mm length. The materials underwent solution heat treatment and subsequent two-step aging treatments using a vacuum furnace with the conditions presented in Table II. For all heat treatments, materials were moved to a cooling chamber and cooled down by thermal radiation. The cooling rate from solution temperature was about 300 K/min. The aging conditions were carefully selected to yield similar average γ' precipitate sizes across the three alloys. Edge lengths along [100] direction of cuboidal γ' precipitates were measured for at least 150 precipitates to determine the average precipitate size of each material.

B. *High-Temperature Tests*

The crystallographic orientation of heat-treated SC bars was measured by the back-reflection Laue method, and the bars with less than 5 deg of longitudinal crystallographic misorientation from $< 001 >$ were selected for a tensile creep test performed in this study. The creep testing specimens have a 4 mm diameter and a 20 mm parallel section, in accordance with the JIS-Z2271 standard.[64] Creep tests were performed following the same standard at 1100 °C/137 MPa, 1000 °C/245 MPa, 900 °C/392 MPa, and 800 °C/735 MPa for all three alloys listed in Table I.

Phase stability and equilibria analyses were performed on the SC billets using the same prolonged aging test method from previous studies.[60,64] The SC billets with a 5 mm thickness were cut from as-heat-treated SC bars. To obtain a time-temperature-transformation (TTT) diagram, the cut-out billets were further exposed in a resistive furnace at 800-1200 °C for up to 1000 hours. To analyze phase equilibria at the creep test temperature, severe plastic deformation was introduced into a billet at room-temperature, followed by annealing at 1100 °C for 500 hours. This strain aging method was applied to the material to enhance recrystallization and faster microstructure evolution, enabling the γ/γ' microstructure to approach equilibrium and become coarse enough to measure their individual composition using microscopy.[65]

C. *Microstructure Observations*

Microstructures of heat-treated, creep-ruptured, and prolong-aged samples were observed using a scanning electron microscopy (SEM). A field emission gun-scanning electron microscope (FEG-SEM), Zeiss Gemini 300, was operated for the observations. Superalloy samples for microstructure observation were mounted into a conductive resin, followed by metallographic polishing to colloidal silica with a 0.05 μm particle size. Because each specimen condition required examination of different microstructural features, the observation plane was varied accordingly. As-heat-treated samples were polished on planes near (001) plane, creep-ruptured specimens were sectioned and polished in the loading direction (crystallographic plane unknown), and prolonged-aged samples were polished on planes parallel to the growth direction.

Creep-ruptured samples were analyzed using electron backscatter electron diffraction (EBSD) by EDAX CMOS camera equipped on the Zeiss Gemini 300 FEG-SEM, with a step of 50 nm. Indexed data were post-processed using EDAX OIM Analysis™ 8. The same FEG-SEM with angular selective backscatter (AsB) detector was used to obtain electron channeling contrast images (ECCIs) operated at an acceleration voltage of 20 kV and probe size of 60 μm. Local compositions of γ and γ' phases were quantitatively measured using an Electron-probe Microanalyzer (EPMA) Shimadzu EPMA-1610 at the recrystallized and coarsened microstructure.

To analyze the effect of γ/γ' interfacial misfit, creep-ruptured samples were observed using a transmission electron microscopy (TEM), JEOL JEM-4010 and JEM-2100. End of the parallel gauge section close to transition radius were cut into discs perpendicular to the loading direction, followed by mechanical polishing for thinning down to < 100 μm. The thinned discs were electrochemically polished by twin jet method (Fischione Instruments) with following conditions: A 40 V electrolytic voltage on a solution of $CH_3COOH:HCO_4 = 10:1$ at a 10 °C solution temperature.

III. RESULTS

A. *Microstructure Before the High-Temperature Tests*

Microstructure after the solution and aging heat treatments was observed using SEM in back scatter electron (BSE) imaging mode as shown in Figure 2. All the experimental alloys have been successfully solution treated and present a microstructure without γ/γ' eutectic pool. All the materials present cuboidal γ' precipitates in general, which have an edge length average of 211.3 nm (TMS-238), 199.5 nm (TMS-238MoRu), and 241.6 nm (TMS-238MoIr) as presented in Figure 3. Unlike standard TMS-238, the conceptual TMS-238MoRu and TMS-238MoIr exhibit thick γ channels (~ 50 nm) and fine γ' precipitates (~ 25 nm) inside these channels. Additionally, in these modified alloys, some precipitates appear to have merged with nearby ones through very thin channels. While the average precipitate sizes are similar across all alloys, these characteristics of precipitates in the conceptual alloys are reflected in error bars in Figure 3. In addition to the γ/γ' phases, TMS-238MoRu and TMS-238MoIr have diagonal traces as shown in Figures 2(b) and (c), respectively, and are surrounded by dotted curves. These areas represent thick γ channels lying on the observation plane, and precipitates beneath this γ-channel layer are exposed due to relatively high acceleration voltage (20 kV).

These γ-channel layers were observed at higher magnification using ECCI and the obtained images shown in Figure 4. Within the thick γ-channels, a substantial number of dislocations and planar faults were observed for both TMS-238MoRu and TMS-238MoIr. Not only were they observed in the matrix, but also some planar faults in the matrix were extending into γ' precipitates (examples are pointed by arrows in Figure 4(d)). These are mainly stacking faults as they lie on the {111} plane and continuously extending from the matrix.[66–68]

B. *Creep Properties of TMS-238 and Concept Variants*

The results of creep tests on the three experimental alloys, TMS-238, TMS-238MoRu, and TMS-238MoIr, at 1100 °C/137 MPa, 1000 °C/245 MPa, 900 °C/

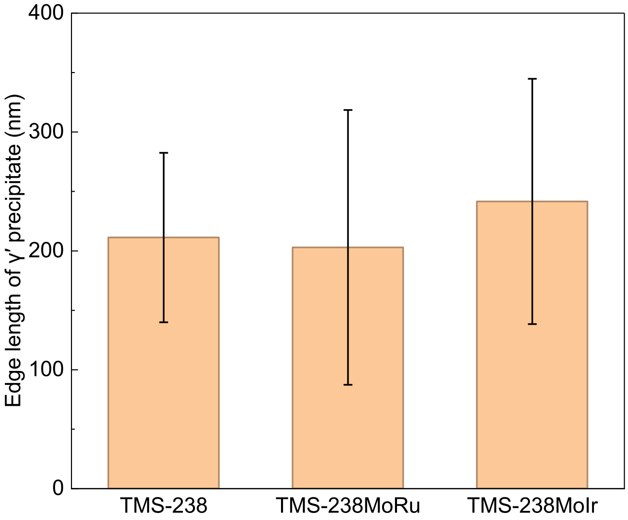

Fig. 3—Edge length of γ' precipitate in the dendritic core region of TMS-238, TMS-238MoRu, and TMS-238MoIr before the high-temperature tests.

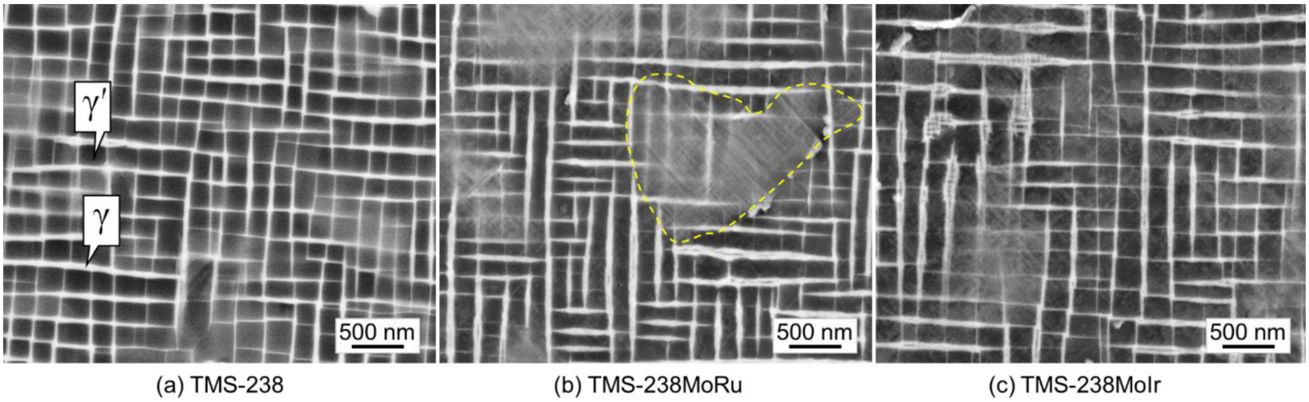

(a) TMS-238 (b) TMS-238MoRu (c) TMS-238MoIr

Fig. 2—SEM-BSE microstructures of TMS-238 (*a*), TMS-238MoRu (*b*), and TMS-238MoIr (*c*) before high-temperature tests. The dotted curve outlines an example of thick γ-channel oriented parallel to the imaging plane close to (001) plane.

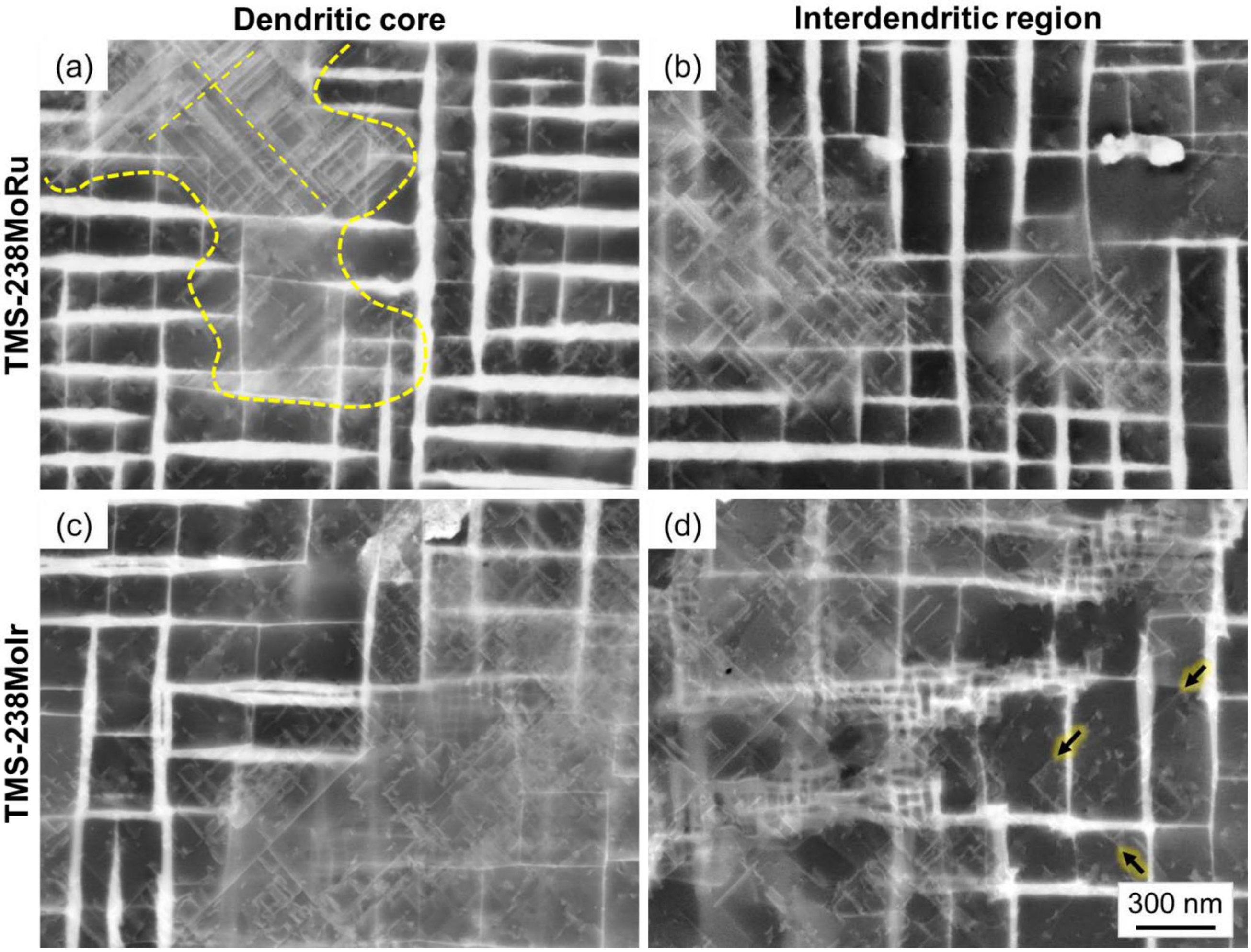

Fig. 4—Detailed microstructures of TMS-238MoRu (*a*), (*b*) and TMS-238MoIr (*c*), (*d*) obtained by ECCI. The dotted curve outlines an example of thick γ channel oriented parallel to the imaging plane and the dotted lines are direction of planar faults inside the thick γ channel. Arrows are pointing at examples of stacking faults in γ' which are extending from the γ channel.

392 MPa, and 800 °C/735 MPa are shown in Figure 5 along with two representative commercial alloys, CMSX-4 and CMSX-10.[5,69] The creep strain rate is plotted against the creep time as shown in Figure 6.

At 1100 °C/137 MPa, compared with baseline TMS-238 (1284 and 1925 hours), TMS-238MoIr demonstrated superior creep durability that can reach up to 4044 hours.[17] As mentioned earlier, this is the longest creep life reported for this condition in the available literature.[17] TMS-238MoIr has very similar creep properties to TMS-238 at 1000 °C/245 MPa; however, this material has about half the life of the baseline at the lower temperature conditions of 900 °C/392 MPa and 800 °C/735 MPa. TMS-238MoRu exhibited the lowest creep life of these three materials in all four conditions tested, underperforming in comparison with the baseline TMS-238.

Creep strain rate curves in Figure 6 explain their differences in detail. At 1100 °C/137 MPa and 1000 °C/245 MPa (Figures 6(a), (b)), TMS-238MoIr and TMS-238 have very similar trend during secondary creep stage, whereas TMS-238MoRu was deforming at higher rate in this stage. At 900 °C/392 MPa and 800 °C/735 MPa (Figures 6(c), (d)), TMS-238MoRu showed immediate transition into the creep accelerating stage in comparison to the other two alloys.

Larson-Miller parameters of TMS-238, TMS-238MoRu, and TMS-238MoIr calculated from their creep rupture life are plotted in Figure 7. Compared to the commercial alloys, CMSX-4 and CMSX-10, TMS-238 has well balanced creep lives for all temperature ranges. Increasing magnitude of negative lattice misfit with suppression of TCP phase, approach tested in this study, has shown effectiveness at creep temperatures above 1000 °C.

C. *Microstructural Analyses After Creep Tests at 1100 °C/137 MPa*

Post-mortem microstructures of creep-ruptured samples were analyzed to investigate the mechanism of the improved and degraded creep properties of TMS-238MoIr and TMS-238MoRu compared to TMS-238 at the targeted condition of at 1100 °C/

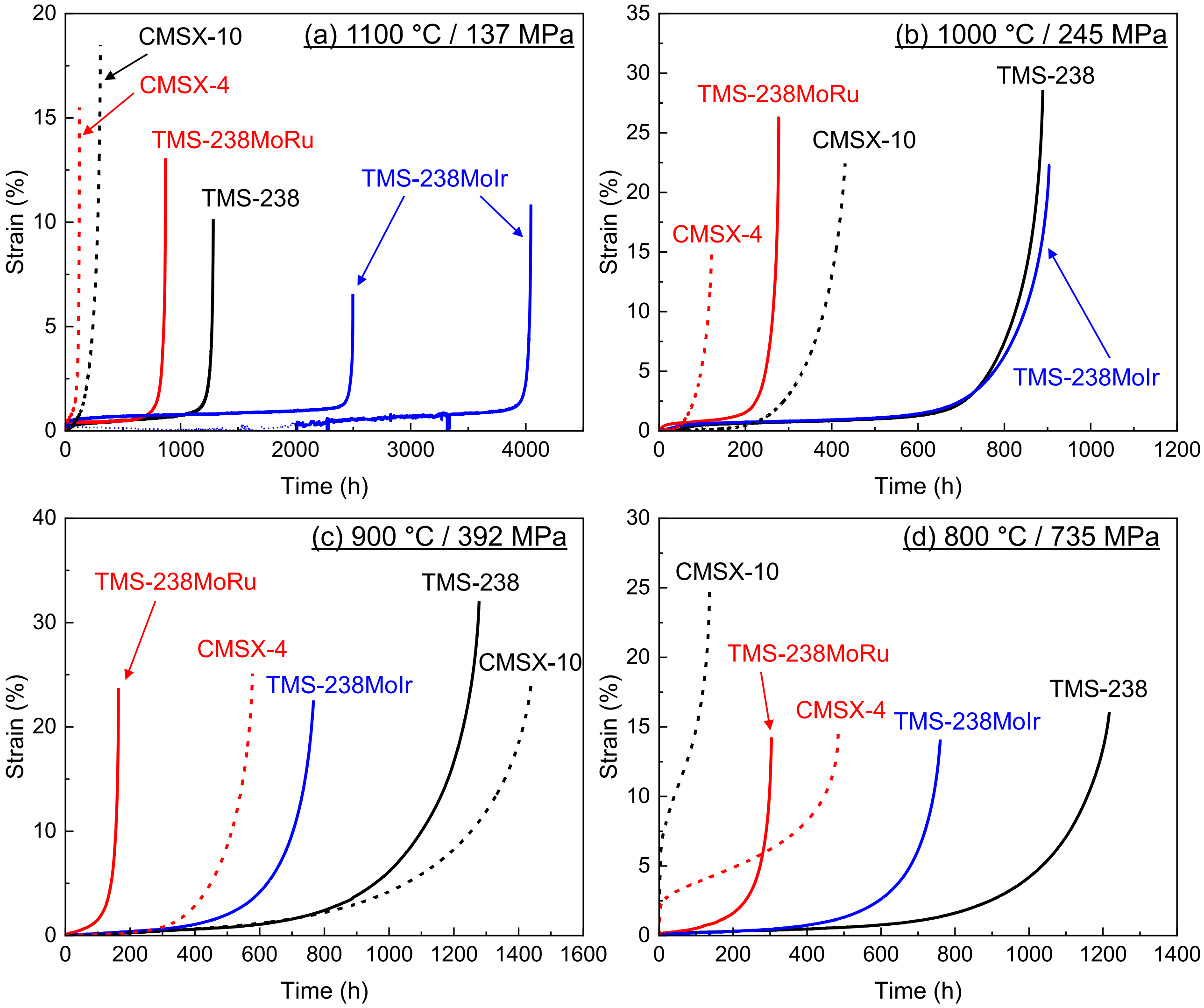

Fig. 5—Creep curves of TMS-238, TMS-238MoRu, and TMS-238MoIr conducted at 1100 °C/137 MPa (*a*), 1000 °C/245 MPa (*b*), 900 °C/392 MPa (*c*), and 800 °C/735 MPa (*d*). Two representative commercials alloys, CMSX-4 and CMSX-10, are included for comparison.

137 MPa. Figure 8 presents the microstructures of each alloy after the creep rupture test at 1100 °C/137 MPa. Figures 8(a) through (c) show the microstructure at the dendritic core located 1 mm away from the fracture surface of TMS-238 (ruptured at 1284 hours), TMS-238MoRu (ruptured at 870 hours), and TMS-238MoIr (ruptured at 4044 hours) samples, respectively. Representative γ'-rafted microstructure of the same samples at the dendritic core close to the gage end (0.5 mm away from the end toward fracture surface) are shown in Figures 8(d) through (f).

The baseline TMS-238 has some TCP precipitates (approximately 0.3 pct by area) that form surrounding γ'-envelope, which can be a path for dislocation glide and climb during the creep deformation. Figure 8(a) is a particular example of creep void growing at γ'-TCP region which is speculated to be accelerated by the γ'-envelope. In contrast, TMS-238MoRu (Figure 8(b)) exhibited a substantial precipitation of TCP phase (area fraction ~ 6.5 pct) and coarsening of γ'-rafts around TCP precipitates. Surprisingly, even after 4000 hours of exposure, only few TCP precipitates were nucleated in TMS-238MoIr that has negligible effect on the creep life and failure processes. The failure mechanism of TMS-238MoIr seemed to be typical nucleation and growth of creep voids (see example in Figure 8(c)). Superior γ/γ' phase stability during the creep testing has been achieved by substitution of Ru by Ir.

γ'-rafted structure shown in Figures 8(d) through (f) are typically observed in Ni-base SC superalloys creep tested at temperatures above 900 °C. Acquisition locations for these images were 0.5 mm from the gage end to avoid effect of severe straining near the fracture surface that can degrade γ'-rafts. In all experimental alloys, a continuous raft structure oriented perpendicular to the stress axis was observed. To compare the γ'-rafts and γ' volume fraction of these materials, SEM-BSE images were analyzed using ImageJ Fiji[70] with Trainable Weka Segmentation[71] and LinearDistance[72] plugins, and the results are shown in Figure 9. The difference of the

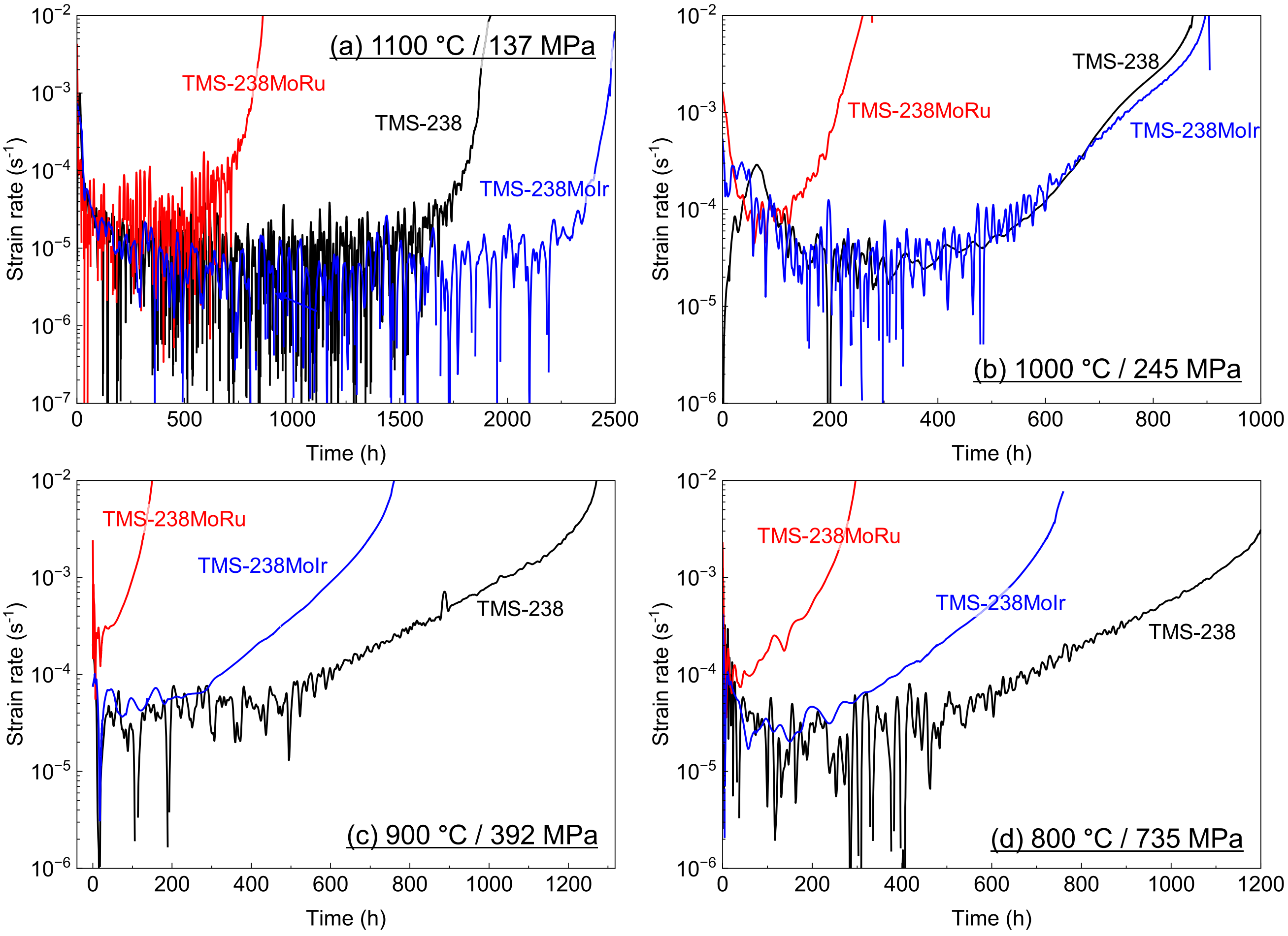

Fig. 6—Creep strain rate curves of TMS-238, TMS-238MoRu, and TMS-238MoIr conducted at 1100 °C/137 MPa (*a*), 1000 °C/245 MPa (*b*), 900 °C/392 MPa (*c*), and 800 °C/735 MPa (*d*).

γ'-rafts between these materials are within the statistical scatter and not significant overall. Volume fraction of γ' phase was higher at the interdendritic area for all the tested material, due to the dendritic segregation. This suggests that the magnitude of segregation was different among the materials; particularly, TMS-238MoIr showed the largest deviation between the primary dendrite core and the interdendritic area, probably by effect of slower diffusion of Ir. Average volume fraction was 64 to 65 pct, which is slightly higher than the estimation by NIMS-ADP (Table I), but consistent for all the materials as expected.

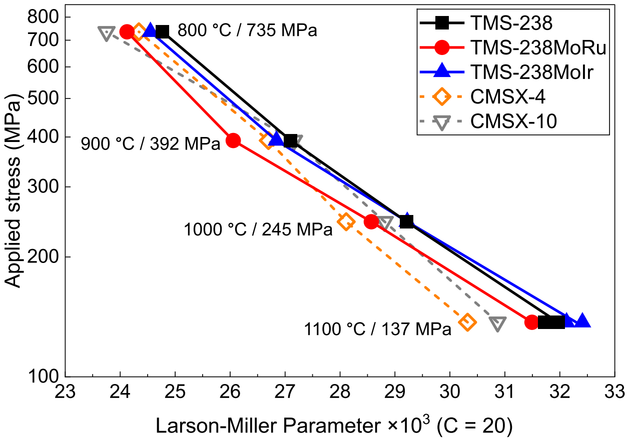

Fig. 7—Larson–Miller plots (C = 20) for Ni-base SC superalloys creep tested in this study.

To validate the concept of strengthening via very high negative γ/γ' lattice misfit, γ/γ' interfacial dislocation networks on the plane perpendicular to the loading direction were examined using TEM, and representative micrographs are shown in Figure 10. Dislocation spacing was quantified using the line-intercept method by counting the intersections between dislocations and lines drawn along the [100] direction, allowing direct comparison of dislocation density.[64,73] A minimum of 70 dislocation segments were measured for statistical reliability, and the results are summarized in Figure 11. The data clearly show a refinement of the interfacial dislocation network in the following order: TMS-238 (38.2 nm), TMS-238MoIr (25.5 nm), and TMS-238MoRu (19.7 nm). These results demonstrate that increasing the magnitude of negative lattice misfit through alloy composition modification (addition of 1.5 at. pct Mo) effectively promotes dislocation network

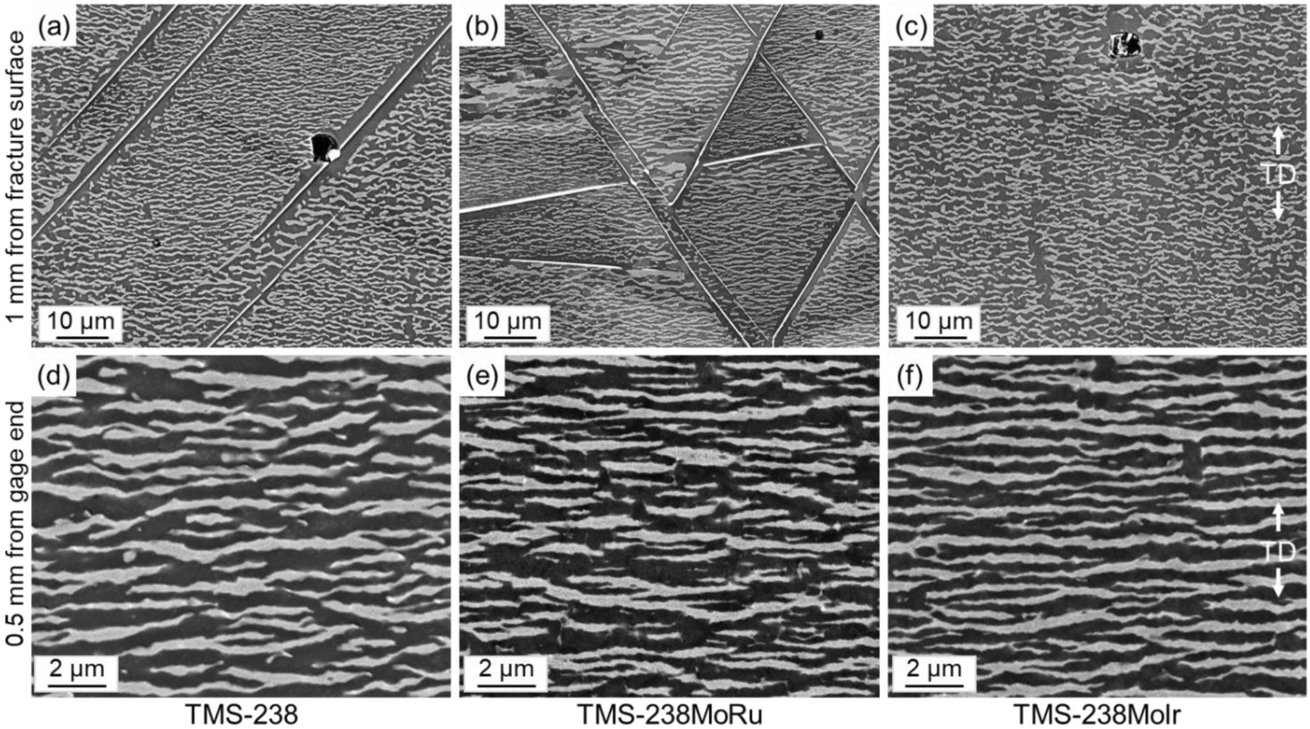

Fig. 8—SEM-BSE images of TMS-238 (*a*), (*d*), TMS-238MoRu (*b*), (*e*), and TMS-238MoIr (*c*), (*f*) samples after creep rupture test at 1100 °C/137 MPa. Observed locations are 1 mm from the fracture surface toward gage end (a) to (c) and 0.5 mm from gage end toward fracture surface (d) to (f).

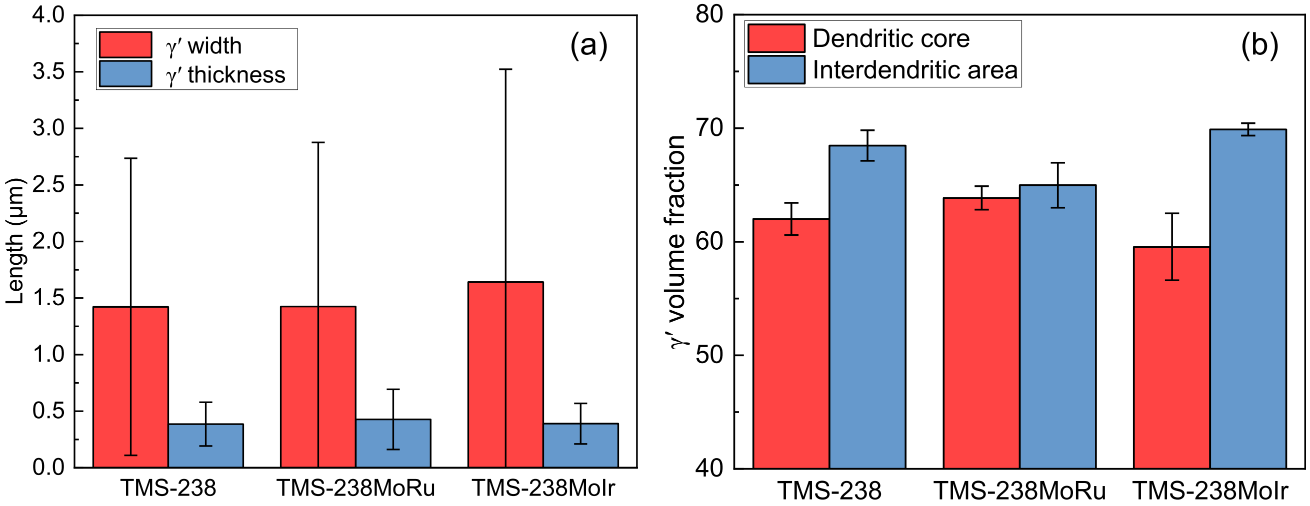

Fig. 9—(*a*) γ'-raft width (perpendicular to the loading axis) and thickness (parallel to the loading axis) and (*b*) γ' volume fraction at primary dendritic core and interdendritic area of TMS-238, TMS-238MoRu, and TMS-238MoIr samples after creep rupture tests at 1100 °C/137 MPa. Error bars represent standard deviation.

refinement. With the combination of γ/γ' microstructure stability, the longest creep life was achieved by TMS-238MoIr.

D. *Microstructural Analyses After Creep Tests at 900 °C/392 MPa*

Contrarily to the successful creep property improvement at 1100 °C/137 MPa by tailoring γ/γ' lattice misfit, creep life of two modified alloys drastically decreased from that of the baseline TMS-238 at 900 °C/392 MPa condition. Microstructures were analyzed using SEM and EBSD to investigate the cause of the creep life reduction.

Color coded inverse pole figure (IPF) maps and grain reference orientation deviation (GROD) maps were obtained from samples after creep rupture tests at 900 °C/392 MPa (Figure 12). The EBSD data was

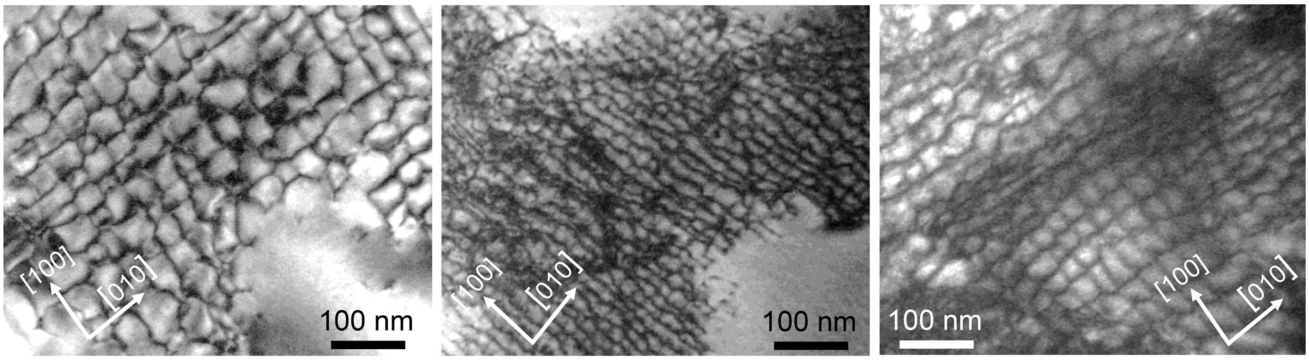

(a) TMS-238 (b) TMS-238MoRu (c) TMS-238MoIr

Fig. 10—TEM micrograph of TMS-238 (*a*), TMS-238MoRu (*b*), and TMS-238MoIr (*c*) samples after creep rupture test at 1100 °C/137 MPa obtained with beam direction parallel to [001] zone axis, showing γ/γ' interfacial dislocation networks.

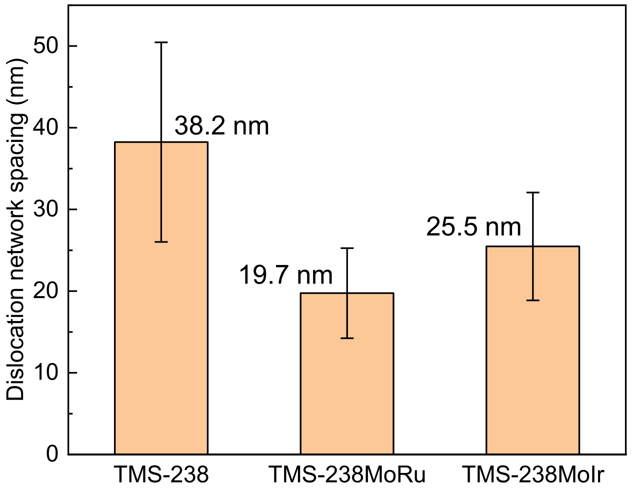

Fig. 11—Average γ/γ' interfacial dislocation network spacing along [100] direction of TMS-238, TMS-238MoRu, and TMS-238MoIr samples after creep rupture tests at 1100 °C/137 MPa. Error bars present standard deviation.

collected around creep void locating 200 μm away from the fracture surface. Notable characteristics of the modified alloys are that TCP precipitates are spreading widely in the microstructure, and chains of recrystallized grains are extending from the edges of the creep voids. In those recrystallized chains, TCP phases are precipitating in granular form (see Figure 13). Isolated void nucleation and crack propagation are observed along the chain of recrystallized grains (see Figure 12(c)). These creep voids and recrystallized chains were observed up to ~ 2 mm away from fracture surface and not at the regions near the gage end. Therefore, void nucleation and recrystallization occurred during the creep acceleration stage of TMS-238MoRu and TMS-238MoIr, and the failure process was by far faster and shorter than that of the baseline TMS-238 (see also creep strain rate in Figure 6(c)).

GROD maps in Figure 12 represent the local crystallographic misorientation within individual grains, calculated with respect to the orientation of a pixel with minimum kernel average misorientation of each grain. GROD quantifies the degree of intragranular lattice distortion, which means the higher GROD misorientation values typically indicate regions of increased plastic deformation. Creep void in TMS-238 is obviously the crack initiation site and higher magnitude of lattice rotation around the void induced twinning. In the alloys with significant TCP precipitation (TMS-238MoRu in Figure 12(d) and TMS-238MoIr in Figure 12(f)), the GROD maps reveal the plastic deformation accumulation at TCP interfaces. This localized deformation likely causes the higher creep strain rates observed in TMS-238MoRu throughout the entire test and earlier onset of tertiary creep in TMS-238MoIr (Figure 6(c)). The local crystallographic misorientation is recovered by the formation of recrystallization chain.

Regions far from the fracture surface were observed and shown in Figure 14. TMS-238MoRu, shown in Figure 14(b), exhibited a fine but higher number of TCP precipitates compared to the other two alloys, which correlates with its significantly reduced creep life. In the higher magnification of microstructure of TMS-238MoIr (Figure 14(d)), TCP phase is precipitating from γ-channel and defects inside the γ' (probably stacking faults) are extending from those TCP precipitates. Shape of γ-channels connected to TCP precipitate are distorted along the growth direction of TCP.

E. *γ/γ' Phase Stability and TCP Phase Precipitation*

As the creep properties of the experimental alloys were affected by TCP phase precipitation, the differences in γ–γ' microstructural stabilization effects resulting from Mo, Ru, and Ir additions in Ni-base superalloy TMS-238 need clarification. The γ–γ' partitioning behavior of alloying elements in TMS-238MoRu and TMS-238MoIr was investigated from an equilibrium perspective, while the isothermal transformation associated with TCP precipitation was examined from a kinetic perspective.

The partition ratio K of alloying elements was defined as $K = X\gamma/X\gamma'$, where $X\gamma$ and $X\gamma'$ represent the chemical composition in the γ phase and γ' phase, respectively. Figure 15 shows the microstructure of TMS-238MoRu and TMS-238MoIr after the strain aging at 1100 °C for 500 hours, having the TCP phase

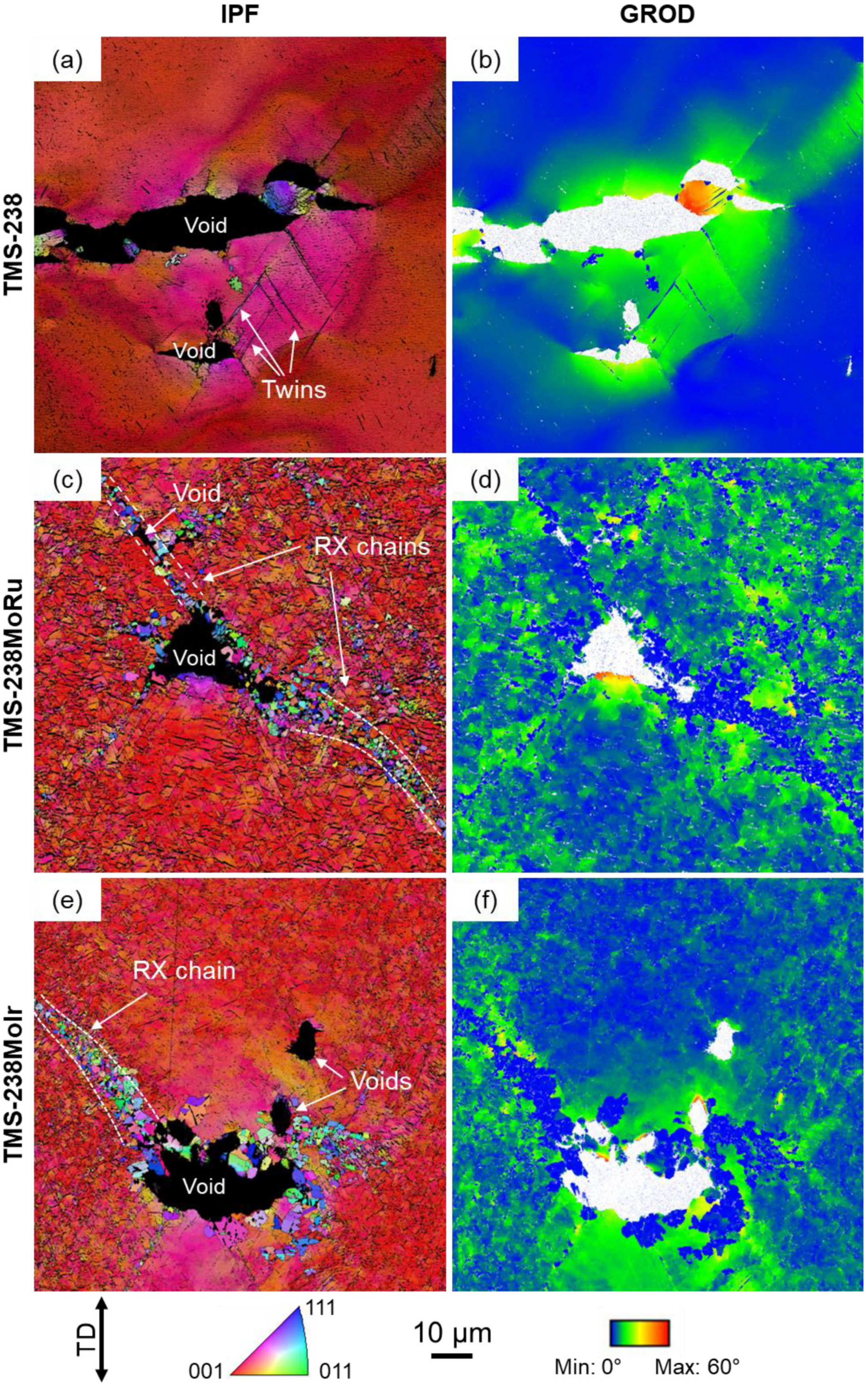
IPF
GROD
TMS-238
(a)
Void
Void
Twins
(b)
TMS-238MoRu
(c)
Void
RX chains
Void
(d)
TMS-238MoIr
(e)
RX chain
Voids
Void
(f)
TD
111
001
011
10 μm
Min: 0°
Max: 60°

◀Fig. 12—IPF color-coded orientation maps referring to the tensile direction (*a*), (*c*), (*e*) and GROD maps respect to the orientation of pixel with minimum kernel average misorientation (*b*), (*d*), (*f*) of TMS-238 (a), (b), TMS-238MoRu (c), (d), and TMS-238MoIr (e), (f) after creep rupture tests at 900 °C/392 MPa. Data were collected at the location 200 μm away from fracture surface. (Color image available online).

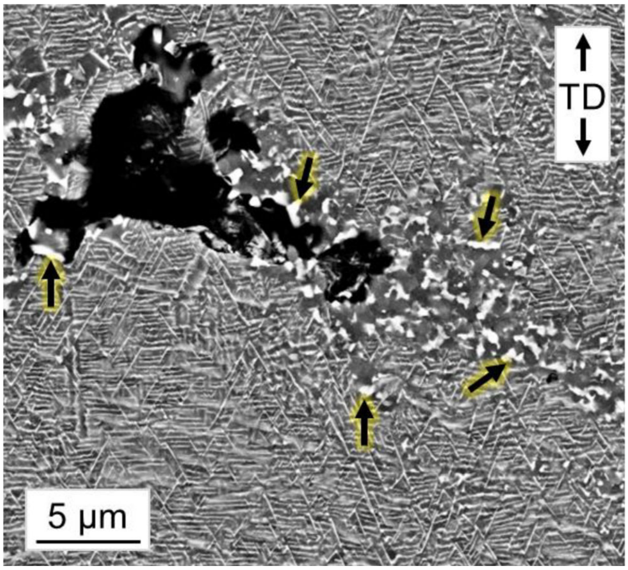

Fig. 13—SEM-BSE image of TMS-238MoRu after creep rupture test at 900 °C/392 MPa (same location as Fig. 11(c), (d)). Arrows are pointing at examples of TCP phase precipitates in the chain of recrystallized grains.

precipitated in both alloys under nearly equilibrium state. Figure 16 presents the partition ratios of the alloying elements between γ and γ', revealing marginal differences in partitioning behavior between TMS-238MoRu and TMS-238MoIr compared to TMS-238. This indicates that, thermodynamically, partitioning of alloying elements does not vary by addition of Mo and Ru or Ir to TMS-238. Overall partitioning trends are similar to those have been reported in the previous studies.[65,74,75]

TTT diagrams for TMS-238MoRu and TMS-238MoIr are presented in Figure 17. In these diagrams, circles and triangles indicate the sampling points for TCP phase precipitation in TMS-238MoRu and TMS-238MoIr, respectively, with filled symbols representing conditions under which TCP phases were observed. The solid curve was drawn based on confirmed TCP precipitation points. For comparison, the TTT diagram for TMS-238 was drawn using data from the previous study.[60] The nose temperature for both TMS-238MoRu and TMS-238MoIr is in between 900 °C and 1000 °C, and the time of first TCP precipitation shifts to shorter aging durations for the TMS-238MoRu. This trend is consistent regardless of observation locations; dendritic core (Figure 17(a)) and interdendritic (Figure 17(b)) regions. In the dendritic core region, TCP phase precipitation in TMS-238MoRu at 900–1000 °C occurred earlier than 50 hours of aging.

From both equilibria and kinetic perspectives, the addition of Mo to TMS-238 promotes TCP phase formation, even in the presence of TCP-suppressing elements such as Ru and Ir. In addition, although both TMS-238MoRu and TMS-238MoIr have higher tendency for early TCP precipitation compared to TMS-238, replacing 2 at. pct of Ru by Ir effectively delays TCP formation, thus stabilizing the γ/γ' microstructure, particularly at temperatures higher than 1050 °C.

IV. DISCUSSION

This discussion focuses on how targeted alloying modifications to the sixth-generation Ni-based single crystal superalloy TMS-238 influence the γ/γ' lattice misfit, and how these changes affect microstructural evolution and creep deformation behaviors at 1100 °C and 900 °C. Particular emphasis is placed on the role of γ/γ' misfit in controlling interfacial dislocation networks and phase stability. The influence of Ir addition—especially in comparison to Ru—is further discussed in the context of its impact on high-temperature properties. These findings are compared to previous studies conducted at NIMS, providing a comprehensive understanding of how elemental partitioning, diffusion behavior, and phase stability interact to control creep performance of Ni-base SC superalloys.

A. *Effect of Alloy Composition Modifications on the γ/γ' Lattice Misfit and the Creep Properties at 1100 °C/137 MPa*

Tailoring the γ/γ' lattice misfit and to densify the interfacial dislocation network is a key strategy for enhancing the high-temperature creep resistance of Ni-base SC superalloys. The observed dislocation network after the creep test showed very fine structure as quantified in Figure 11. This confirms that the concept alloys with addition of 1.5 at. pct Mo have increased the magnitude of negative lattice misfit, particularly effective in the case for TMS-238MoRu with the smallest dislocation spacings. The elemental partitioning side of Mo in both TMS-238MoRu and TMS-238MoIr did not change by addition of Ru or Ir (see Figure 16). TMS-238MoRu had the highest partition coefficient of Mo to γ among three alloys, and Ru also preferentially partitions into γ side; both can contribute to increasing lattice constant of γ phase.[50,58,59,76–78] The Ir partitioning to γ' observed in TMS-238MoIr, similar trend reported in the literature, possibly increased the lattice constant of γ', leading to slightly coarser interfacial dislocation network of this alloy.[74–77,79]

The primary creep stage of the creep curves from the creep tests at 1100 °C/137 MPa is shown in Figure 18. The time required to reach the steady-state creep region from the onset of creep was shortest for TMS-238MoRu, followed by TMS-238MoIr and TMS-238. These results are consistent with previous reports explaining the relationship that a more negative lattice misfit accelerates γ/γ' phase rafting, and therefore,

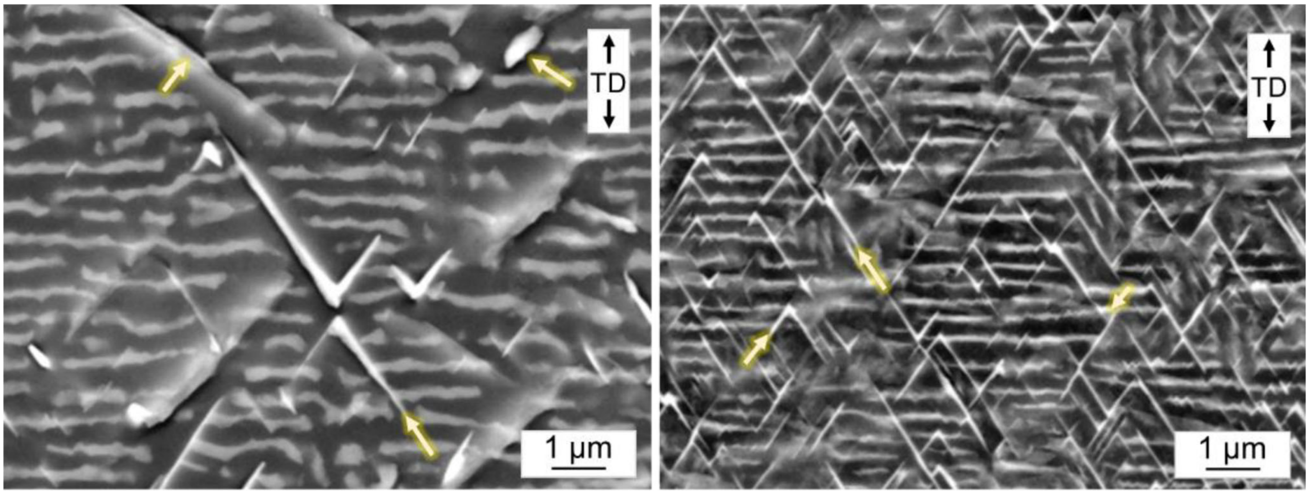

(a) TMS-238 (b) TMS-238MoRu

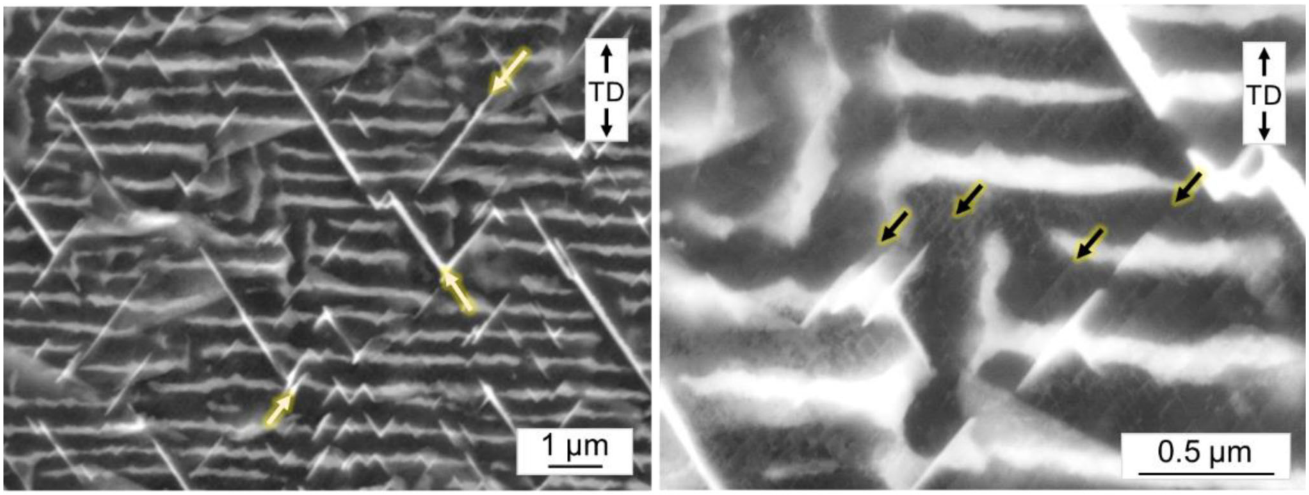

(c) TMS-238MoIr (d) TMS-238MoIr

Fig. 14—SEM-BSE images of TMS-238 (*a*), TMS-238MoRu (*b*), and TMS-238MoIr (*c*) after creep rupture test at 900 °C/392 MPa. Images were taken at dendritic core region located 0.5 mm from gage end toward fracture surface. (*d*) Is detailed image of (c) obtained by ECCI and arrows in this image indicate defects extending from TCP precipitates.

the primary creep stage finishes earlier. Normally in the Ni-base SC superalloys, morphology of γ'-raft also depends on the γ/γ' lattice misfit and initial γ' precipitate size, which influence the microstructure evolution during the primary creep stage at temperatures above 1000 °C.[46,80,81] The perfection degree (aspect ratio) of γ'-raft is important for creep life since the smoother and longer γ'-raft means wider net area of horizontal γ/γ' interface that limits dislocation path.[46] However, the quantified width and thickness of γ'-raft were almost the same for all the tested alloys (see Figure 9), and therefore the perfection degree of the γ'-raft did not contribute to the varying creep life. It is worth noting that γ'-rafts observed in this study are by far thinner than those in other commercial superalloys reported previously. This suggests that the dislocation network density is one of dominant factors determining creep durability of these alloys. The exceptional creep life of 4044 hours of TMS-238MoIr at 1100 °C/137 MPa can therefore be attributed to the synergistic effect of a high γ/γ' lattice misfit and improved γ/γ' phase stability that prevented TCP phase precipitation.

Extremely high magnitude of γ/γ' lattice misfit also influenced the microstructure before the creep tests. With 0.3 pct misfit (normally seen for commercial alloys with 3–5 wt pct Re), the expected γ/γ' coherency stress arising from the lattice misfit can be up to 350 MPa.[82,83] TMS-238MoRu has dislocation spacing of ~ 20 nm, which is nearly half of TMS-238 (see Figure 11). The relationship between absolute value of lattice misfit δ, dislocation network spacing d, and magnitude of Burgers vector b can be simplified in the following Eq. [1][78,84]:

$$|\delta| = |b|/d \qquad [1]$$

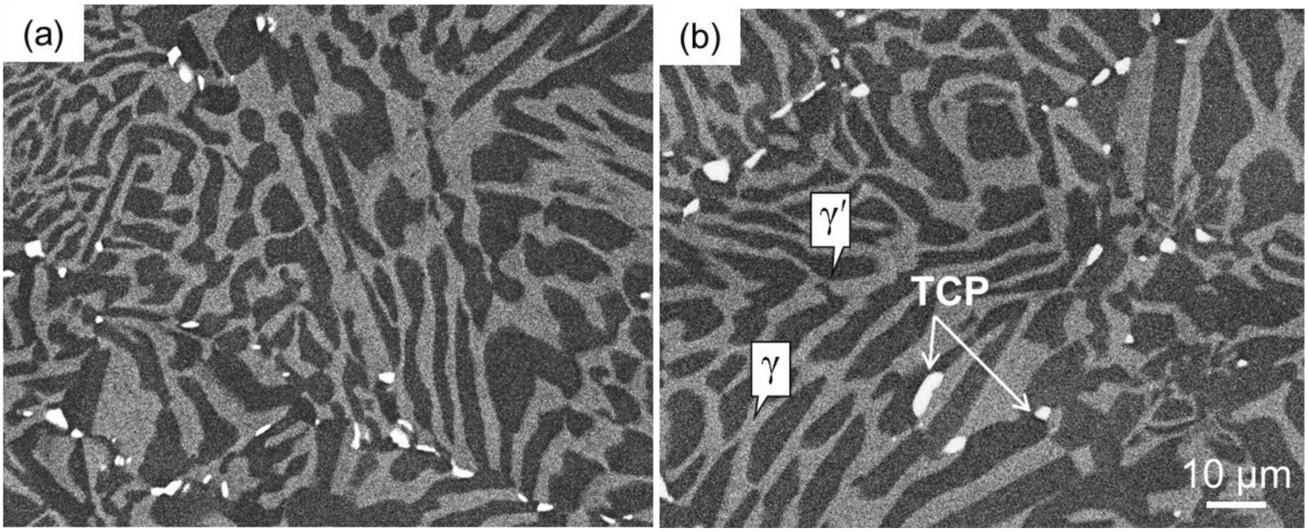

Fig. 15—SEM-BSE images of TMS-238MoRu (*a*) and TMS-238MoIr (*b*) after strain aging at 1100 °C—500 h, showing γ/γ' and TCP phases.

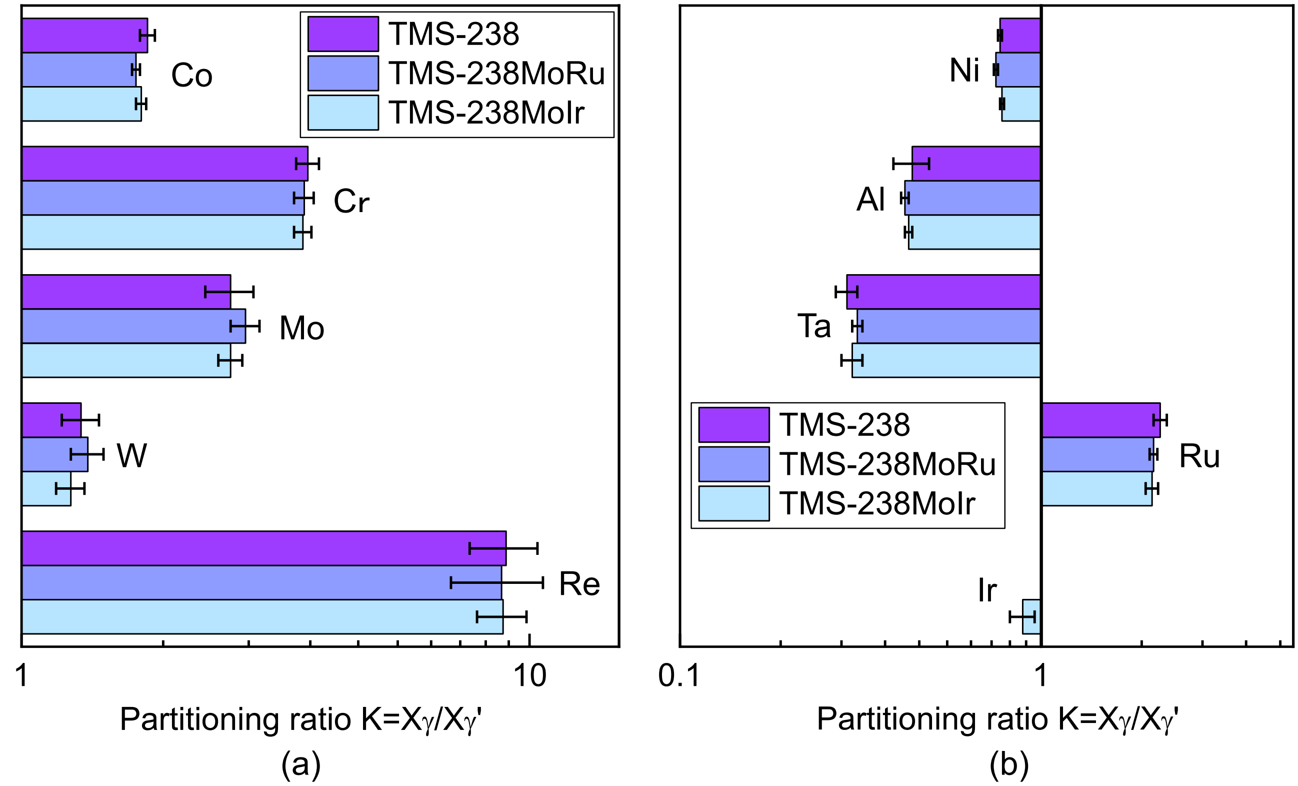

Fig. 16—Elemental partitioning ratios for alloying elements favoring partition into the γ phase (*a*) and the γ' phase (*b*), based on compositional analysis of samples strain-aged at 1100 °C for 500 h followed by EPMA. Partitioning ratios of Ru and Ir are included in (b).

With a rough assumption that magnitude of Burgers vector for edge component is similar for TMS-238 and TMS-238MoRu, the γ/γ' lattice misfit of TMS-238MoRu is estimated to be nearly twice of TMS-238 because the dislocation spacing is about the half (Note that the misfit values in Table I are estimations from NIMS-ADP and are not derived from an experimental result). Therefore, much higher coherency stress at the γ/γ' interface is expected for the alloys with Mo addition. At the aging temperature of 870 °C, volume fraction of γ' is nearly maximum level and the compressive stress in the γ matrix is expected to increase drastically.

Moreover, increasing Mo and Ru content naturally decreases stacking fault energy of γ phase.[85–87] Both coherency stress and decreased stacking fault energy

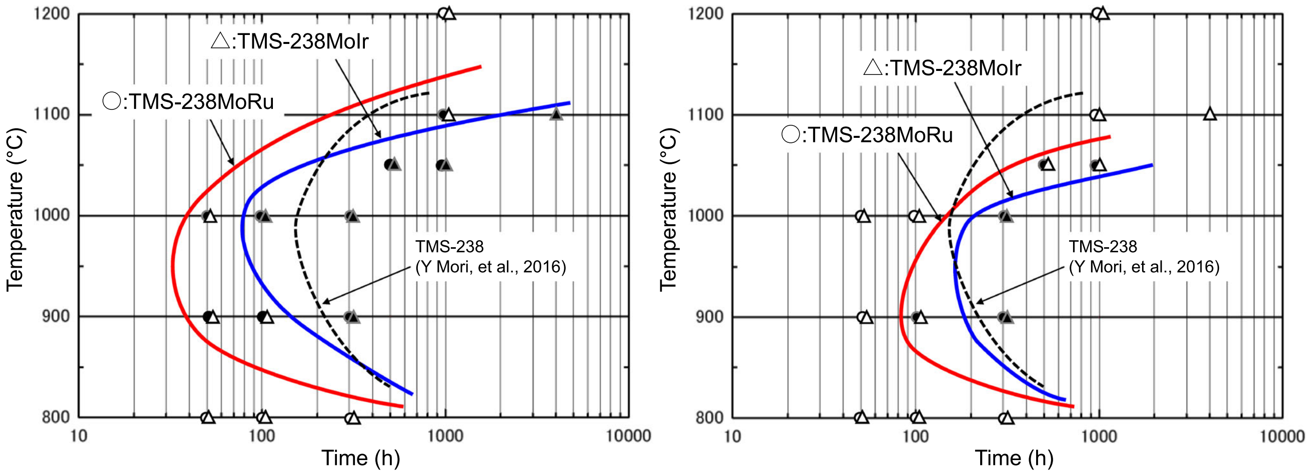

(a) Dendritic core region (b) Interdendritic region

Fig. 17—Time–temperature–transformation (TTT) diagrams for TCP phase precipitation in TMS-238MoRu and TMS-238MoIr, microstructure observed at dendritic core (*a*) and interdendritic (*b*) regions. The TTT curve for TMS-238 is included for reference, based on data from Ref.[60] Circles and triangles indicate sampling points for TMS-238MoRu and TMS-238MoIr, respectively; filled symbols represent conditions where TCP phases were observed.

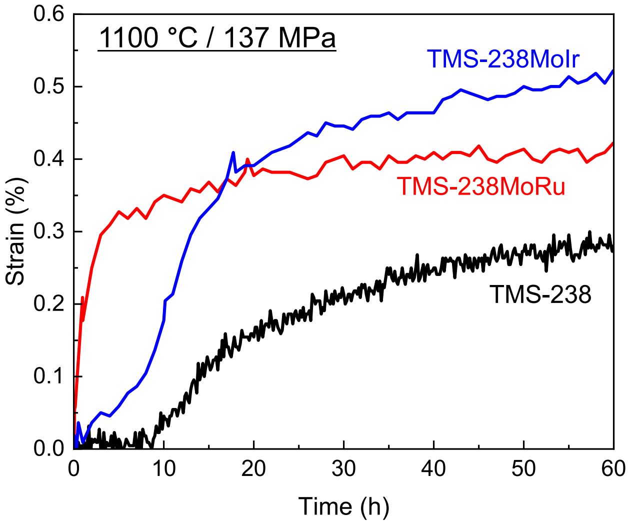

Fig. 18—Initial creep strain evolution of TMS-238, TMS-238MoRu, and TMS-238MoIr alloys tested at 1100 °C/137 MPa, highlighting the transition from primary to steady-state creep behavior.

contributed to the formation of stacking faults inside the matrix observed by ECCI in Figure 4. Matrix channels have variation of thicknesses; however, the stacking faults extending from very thin channel (as thin as 10 nm) can be observed in the same Figure 4. Although Mo and Ru are known to decrease the stacking fault energy, the formation of stacking faults in the as-heat-treated condition (before mechanical loading) has not been previously reported. This suggests that coherency stress plays a significant role in the generation of these stacking faults.

While pre-existing faults may accelerate the transition from primary to secondary creep stage, they should not affect the creep deformation behaviors when the γ'-rafting occurs rapidly (such as > 1100 °C). This is because matrix plasticity is a natural process that first occurs during the primary creep stage. Hence, the relaxation of these planar faults or matrix dislocations into the interfacial dislocation network will progress anyway.[88–90]

B. *Influence of Ru and Ir on the γ/γ' Phase Stability, TCP Formation, and Creep Properties of Ni-Base SC Superalloy*

Among PGMs, Ir has an ability to suppress the precipitation of TCP phases when substituted for Ru in Ni-base SC superalloys.[50,65,91] Notably, Ir has a superior TCP suppression effect in TMS-238 compared to Ru.[60,79] Based on results in the present study, the suppression of TCP phase precipitation in TMS-238MoIr is attributable not to a change of thermodynamic equilibrium such as improvement of solubility limit in Ni-base superalloys by Ir addition, but rather reducing elemental mobility by very low diffusivity of Ir in Ni alloys than other elements.[92,93] This is also consistent in the case where Ru of TMS-238 was simply replaced by Ir.[60,74] Thus, the superior creep rupture life of TMS-238MoIr at 1100 °C/137 MPa derives from the combined effects of increased negative lattice misfit by Mo addition that leads to the formation of a refined γ–γ' interfacial dislocation network induced and enhanced microstructural stability provided by Ir addition. Slower diffusion of Ir itself among alloying elements can also contribute to improving the creep life.[92,93] In contrast, formation of long and extending TCP precipitates during the creep of TMS-238MoRu (see Figure 8(b)) likely accounts for its reduced creep rupture life at the same condition 1100 °C/137 MPa.

At 1000 °C/245 MPa, the benefits of the Ir addition were less pronounced, with TMS-238MoIr exhibiting creep life merely comparable to the baseline TMS-238. This intermediate performance can be due to the dendritic segregation dependent phase stability. While

TCP precipitation was widespread in TMS-238MoRu, it was confined to the dendritic core regions in TMS-238MoIr (microstructural analyses of creep-ruptured samples, not shown here). This TCP precipitate distribution is consistent with the TTT diagrams (Figure 17). This suggests that while the kinetic suppression by Ir is effective in the interdendritic regions at this temperature, it is insufficient to prevent TCP nucleation in the dendritic cores where the segregation of Re is stronger.

Previous studies have shown that the slower diffusion of Ir and its ability to delay TCP phase formation can contribute to improving the creep rupture life of Ni-base SC superalloys at intermediate temperature conditions, such as 900 °C/392 MPa.[74,79] However, this was not the case in the present study due to the severe TCP phase precipitation, as observed in Figures 13 and 14. The primary reason for this is the lack of matrix solubility caused by the high Mo content, as suggested by high SI value listed in Table I. Another likely reason is the initial microstructure, which contained a high density of stacking faults (Figure 4). These faults lie on {111} planes, which are also the preferred crystallographic planes for TCP precipitate growth. The post-mortem microstructure reveals that TCP phases and γ'-shearing faults are on the same crystallographic planes (see Figure 14(d)). Considering that atom probe studies that have shown the segregation of solutes such as Re and W at faults,[94–96] it is plausible that these stacking faults and associated planar faults in γ' precipitates should favor similar segregation, and consequently facilitates TCP nucleation and growth from stacking faults in γ matrix.[97] Therefore, extremely high lattice misfit and decreased stacking fault energy adversely affected the creep properties of the material. This detrimental mechanism appears to be activated at the creep temperatures below 900 °C (including creep test at 800 °C/735 MPa), where the temperature is too low for significant relaxation via γ'-rafting. Furthermore, under these creep conditions, the high applied stress promotes extension of pre-existing planar faults into the γ' phase, accelerating the onset of tertiary creep and leading to premature failure.

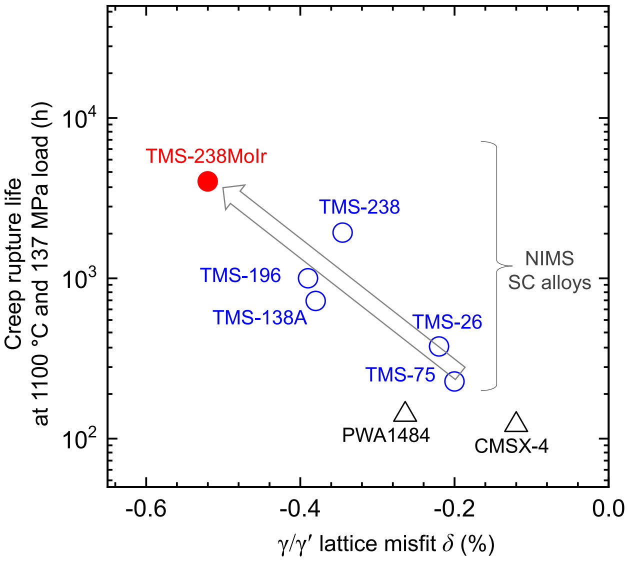

Fig. 19—Relationship between γ/γ' lattice misfit and creep rupture life at 1100 °C/137 MPa. TMS-238MoIr exhibits an excellent creep rupture life beyond TMS-238.

C. *Ni-Base SC Superalloy Design Including Ir*

Figure 19 summarizes the relationship between the misfit and creep rupture life at 1100 °C and 137 MPa for first to sixth-generation Ni-base SC superalloys. The misfit of TMS-238MoIr was estimated by using the same Eq. (1). The circles represent alloys developed in NIMS and the triangles represent commercial alloys. The trend of the magnitude of the negative lattice misfit and creep rupture life under high-temperature and low-stress conditions are consistent for the conceptual TMS-238MoIr alloy presented here. TMS-238MoRu with even higher magnitude of the misfit does not follow the trend. This is because of unstable microstructure with TCP precipitates. This observed trend—achieving a higher lattice misfit requires Mo addition, which in turn increases the risk of TCP formation—is consistent with the findings of Bezold *et al.*[88]

Unbalanced creep properties are because of high Mo content for improving lattice misfit and decreasing stacking fault energy, which induces high risk of TCP, and hence the creep performance at lower temperature cannot be sustained. Ir on the other hand, has shown ability not only to prevent TCP formation, but also to improve creep performance at intermediate to lower temperatures by decreasing diffusivity and increasing solid solution effect.[74,79,98] Further studies are necessary to optimize the materials' creep properties across temperature ranges.

It needs to be mentioned that critical problems of this material are material cost (150 USD/g[99]) and density (approximately 9.37 g/cm^3 for TMS-238MoIr by ADP, see Table I). However, studies on Ni-base superalloys with Ir for both blade alloy and coating applications have shown very small addition of Ir improves oxidation and corrosion resistances.[100,101] Ir indeed has positive effect on the high-temperature properties of Ni-base SC superalloys in overall. Therefore, further optimization may open a door for future application of this class of material.

V. CONCLUSION

Targeting the improvement of high-temperature low-stress creep properties of sixth-generation Ni-base single crystal superalloy TMS-238, TMS-238MoIr (TMS-238 + 1.5 at. pct Mo + 2 at. pct Ir) was previously developed and demonstrated the world's longest creep life of 4044 hours at 1100 °C/137 MPa. This study prepared counterpart alloy TMS-238MoRu (TMS-238 + 1.5 at. pct Mo + 2 at. pct Ru) to investigate creep properties and γ/γ' phase stability of the three alloys including baseline TMS-238. The following main conclusions can be established:

- In contrast to TMS-238MoIr, which exhibited the highest temperature capability of 1136 °C, which is beyond that of TMS-238 at 1120 °C (Larson–Millar conversion by 1000 hours rupture life under 137 MPa), TMS-238MoRu underwent extensive TCP phase precipitation and showed a significantly reduced creep life of 870 hours—about half that of TMS-238.
- Both concept alloys, TMS-238MoRu and TMS-238MoIr, developed exceptionally fine γ/γ' interfacial dislocation networks at 1100 °C/137 MPa, indicating a higher magnitude of negative lattice misfit. This was achieved through the addition of 1.5 at. pct Mo, which preferentially partitions into γ matrix. Suppression of TCP precipitates by Ir addition and improving lattice misfit strengthening by Mo addition are the reasons for TMS-238MoIr exhibiting the best creep life at 1100 °C/137 MPa.
- The underperformance of TMS-238MoRu compared to the baseline TMS-238 was more pronounced under lower temperature creep conditions between 800 °C and 1000 °C. While TMS-238MoIr has comparable creep life to TMS-238 at 1000 °C/245 MPa, this material also showed inferior creep performance at 900 °C/392 MPa and 800 °C/735 MPa.
- A high density of stacking faults was observed in the γ matrix of TMS-238MoRu and TMS-238MoIr, even in the absence of external load. These faults likely formed during the heat treatment due to the combining effect of decreased stacking fault energy by Mo addition, and large coherency stress by exceptionally large lattice misfit. Such defects may have facilitated TCP nucleation at 900–1000 °C as they lie on the same $\{111\}$ crystallographic plane as TCP phases, and serve as segregation sites for TCP-forming solutes such as Re and W.
- Post-creep microstructural analyses and Time-Temperature-Transformation (TTT) diagrams revealed that Ir has a stronger TCP suppression effect than Ru. On the other hand, the detrimental effect of excessive Ru addition was evident, as TMS-238MoRu showed severe TCP precipitation during creep tests at temperatures below 1000 °C, resulting in a creep rupture life shorter than the baseline TMS-238. The TCP precipitates acted as deformation sources during creep loading, and initiated a chain of recrystallization from creep voids, which subsequently served as crack propagation paths.

ACKNOWLEDGMENTS

The authors are grateful to Mariko Iguchi, Kayoko Nakakita, and Megumi Noro (Research Center for Structural Materials, NIMS) for technical assistance with the sample preparation and microstructure observations. A part of this work was supported by the NIMS Microstructural Characterization Platform (NMCP) as a program of the "Nanotechnology Platform" of the Ministry of Education, Culture, Sports, Science and Technology (MEXT), Japan. We are grateful to N. Isaka, NMCP, NIMS, and K. Ogawa, Vibration Control Materials Group, NIMS, for technical support in the TEM observation. This research was financially supported by Japan Science and Technology (JST), under the Advanced Low Carbon Technology Research and Development Program (ALCA) project "Development of direct and complete recycling method for superalloy turbine aerofoils." Grant Number JPNJAL1302.

OPEN ACCESS

REFERENCES

1. H. Harada, High temperature materials for gas turbines: the present and future, in: *Proc. Int. Gas Turbine Congr.*, 2003 Tokyo, Tokyo, 2003: pp. 1–6.
2. R.C. Reed: *The Superalloys: Fundamentals and Applications*, Cambridge University Press, Cambridge, 2006.
3. J.-Y. Guédou and L. Rémy: Past, present, and future of SX superalloys, in *Nickel Base Single Crystals. Length Scales*. G. Cailletaud, J. Cormier, G. Eggeler, V. Maurel, and L. Nazé, eds., Elsevier, Amsterdam, 2022, pp. 3–19.
4. H. Long, S. Mao, Y. Liu, Z. Zhang, and X. Han: *J. Alloys Compd.*, 2018, vol. 743, pp. 203–20. https://doi.org/10.1016/j.jallcom.2018.01.224.
5. G.L. Erickson, The Development and Application of CMSX®-10, in: *Superalloys*, 1996, pp. 35–44. https://doi.org/10.7449/1996/Superalloys_1996_35_44.pdf.
6. W.S. Walston, J.C. Schaeffer, W.H. Murphy, *A New Type of Micorstructual Stability in Superalloys - SRZ, Superalloys* (1996) 9–18.
7. C.M. Austin, R. Darolia, K.S. O'Hara, E.W. Ross, Nickel-based single crystal superalloy and method of making, US5151249A, 1992. https://patents.google.com/patent/US5151249A/en?oq=us5151249. Accessed 6 Jan 2025.
8. J.B. Wahl, K. Harris, CMSX-4 Plus Single Crystal Alloy Development, Characterization and Application Development, in: Superalloys 2016, John Wiley & Sons, Inc., 2016: pp. 25–33. https://doi.org/10.1002/9781119075646.ch3.
9. K. Kawagishi, T. Yokokawa, T. Kobayashi, Y. Koizumi, M. Sakamoto, M. Yuyama, H. Harada, I. Okada, M. Taneike, H. Oguma, Development of low or zero-rhenium high-performance Ni-base single crystal superalloys for jet engine and power

generation applications, in: Superalloys 2016, 2016: pp. 115–122. https://doi.org/10.1002/9781119075646.ch13.

10. J.R. Li, S.Z. Liu, X.G. Wang, Z.X. Shi, J.Q. Zhao, Development of a low-cost third generation single crystal superalloy DD9, in: Superalloys 2016, 2016: pp. 55–63.
11. K. Kawagishi, R. Zhu, T. Yokokawa, T. Kobayashi, Y. Koizumi, M. Yuyama, H. Harada, Development of Low Rhenium 2nd Generation Single Crystal Superalloys with Optimum Environmental and Mechanical Properties, in: 10th Liege Conf. Mater. Adv. Power Eng. 2014, Liège, Belgium, 2014: pp. 532–37.
12. J. Rame, E. Menou, D. Locq, Y. Cosquer, A. Saboundji, M. Perrut, Computational Design and Experimental Characterization of a Novel Third-Generation Single Crystal Superalloy with Balanced High-Temperature Creep Strength and Oxidation Resistance, in: J. Cormier, I. Edmonds, S. Forsik, P. Kontis, C. O'Connell, T. Smith, A. Suzuki, S. Tin, J. Zhang (Eds.), Superalloys 2024, Springer Nature Switzerland, Cham, 2024: pp. 64–72. https://doi.org/10.1007/978-3-031-63937-1_6.
13. K. Kawagishi, A. Yeh, T. Yokokawa, T. Kobayashi, Y. Koizumi, H. Harada, Development of an Oxidation-resistant High-Strength Sixth-Generation Single-Crystal Superalloy TMS-238, in: Superalloys 2012, 2012: pp. 189–95. https://doi.org/10.1002/9781118516430.ch21.
14. H. Harada, H. Murakami, Design of Ni-Base Superalloys, in: T. Saito (Ed.), Comput. Mater. Des., Springer Berlin Heidelberg, Berlin, Heidelberg, 1999: pp. 39–70. https://doi.org/10.1007/978-3-662-03923-6_2.
15. T. Yamagata, H. Harada, S. Nakazawa, M. Yamazaki, Y.G. Nakagawa, Alloy Design for high Strength Ni-base Single Crystal Alloys, in: Superalloys 1984, 1984: pp. 157–66. https://doi.org/10.7449/1984/Superalloys_1984_157_166.
16. H. Harada, K. Ohno, T. Yamagata, T. Yokokawa, M. Yamazaki, Phase Calculation and its Use in Alloy Design Program for Nickel-Base Superalloys, in: Superalloys, 1988: pp. 733–42.
17. T. Yokokawa, H. Harada, K. Kawagishi, T. Kobayashi, M. Yuyama, Development of Next Generation Ni-base Single Crystal Superalloy Containing Ir—Towards 1150°C Temperature Capability—, in: Proc 44th Annu Conf GTSJ Sakata Jpn., Gas Turbine Society of Japan, Sakata, Yamagata, Japan, 2016: pp. 195–98.
18. S. Utada, J. Rame, S. Hamadi, J. Delautre, L. Mataveli Suave, P. Villechaise, J. Cormier, High-temperature pre-deformation and rejuvenation treatment on the microstructure and creep properties of Ni-based single crystal superalloys, in: S. Tin, M. Hardy, J. Clews, J. Cormier, Q. Feng, J. Marcin, C. O'Brien, A. Suzuki (Eds.), Superalloys 2020, Springer International Publishing, 2020: pp. 240–52. https://doi.org/10.1007/978-3-030-51834-9_23.
19. J. Cormier, X. Milhet, J.-L. Champion, and J. Mendez: *Adv. Eng. Mater.*, 2008, vol. 10, pp. 56–61. https://doi.org/10.1002/adem.200700248.
20. X. Guo, W. Zheng, C. Xiao, L. Li, S. Antonov, Y. Zheng, and Q. Feng: *Eng. Fail. Anal.*, 2019, vol. 103, pp. 308–18. https://doi.org/10.1016/j.engfailanal.2019.04.021.
21. Guidance for 30-second and 2-minute one-engine-inoperative (OEI) ratings for rotercraft turbine engines, in: Advis. Circ., Federal Aviation Administration, 2009: pp. 33–7A.
22. A. Epishin, B. Fedelich, G. Nolze, S. Schriever, T. Feldmann, M.F. Ijaz, B. Viguier, D. Poquillon, Y. Le Bouar, A. Ruffini, and A. Finel: *Metall. Mater. Trans. A*, 2018, vol. 49A, pp. 3973–87. https://doi.org/10.1007/s11661-018-4729-6.
23. Y. Ru, H. Zhang, Y. Pei, S. Li, X. Zhao, S. Gong, and H. Xu: *Scr. Mater.*, 2018, vol. 147, pp. 21–26. https://doi.org/10.1016/j.scriptamat.2017.12.023.
24. X.P. Tan, J.L. Liu, T. Jin, Z.Q. Hu, H.U. Hong, B.G. Choi, I.S. Kim, C.Y. Jo, and D. Mangelinck: *Mater. Sci. Eng. A*, 2013, vol. 580, pp. 21–35. https://doi.org/10.1016/j.msea.2013.05.028.
25. A.I. Epishin, B. Fedelich, B. Viguier, S. Schriever, I.L. Svetlov, N.V. Petrushin, R. Saillard, A. Proietti, D. Poquillon, and A. Chyrkin: *Mater. Sci. Eng. A*, 2021, https://doi.org/10.1016/j.msea.2021.141880.
26. S. Utada, L. Després, and J. Cormier: *Metals*, 2021, vol. 11, p. 1610. https://doi.org/10.3390/met11101610.
27. L. Luo, Y. Ru, Y. Ma, S. Li, and S. Gong: *Mater. Sci. Eng. A*, 2022, vol. 832, 142494. https://doi.org/10.1016/j.msea.2021.142494.
28. F. Pedraza and S. Utada: Refurbishment, in *Nickel Base Single Crystal. Length Scales*. G. Cailletaud, J. Cormier, G. Eggeler, and V. Maurel, eds., Elsevier, Amsterdam, 2022, pp. 259–81.
29. S. Utada, Y. Joh, M. Osawa, T. Yokokawa, T. Kobayashi, K. Kawagishi, S. Suzuki, H. Harada, High temperature properties of a single crystal superalloy PWA1484 directly recycled after turbine blade use, in: M. Hardy, E. Huron, U. Glatzel, B. Griffin, B. Lewis, C. Rae, V. Seetharaman, S. Tin (Eds.), *Proc. Int. Symp. Superalloys*, 2016: pp. 591–99. https://doi.org/10.1002/9781119075646.ch63.
30. I.M. Edmonds, S.R. Gregson, N.E. Glover, M.C. Hardy, and I.E. Mitchell: Sustainability and Lifecycle Management of Nickel Superalloy Gas Turbine Components, in *Superalloys 2024*. J. Cormier, I. Edmonds, S. Forsik, P. Kontis, C. O'Connell, T. Smith, A. Suzuki, S. Tin, and J. Zhang, eds., Springer, Cham, 2024, pp. 3–14.
31. J. Rame and S. Utada: L.M. Bortoluci Ormastroni, L. Mataveli Suave, E. Menou, L. Després, P. Kontis, J. Cormier, Platinum containing new generation nickel-based superalloy for single crystalline application, in *Superalloys 2020*. S. Tin, M. Hardy, J. Clews, J. Cormier, Q. Feng, J. Marcin, C. Brien, and A. Suzuki, eds., Springer, Cham, 2020, pp. 71–81.
32. L.M. Bortoluci Ormastroni, S. Utada, J. Rame, L. Mataveli Suave, K. Kawagishi, H. Harada, P. Villechaise, and J. Cormier: Tensile, low cycle fatigue and very high cycle fatigue characterizations of advanced single crystal nickel-based superalloys, in *Superalloys 2020*. S. Tin, M. Hardy, J. Clews, J. Cormier, Q. Feng, J. Marcin, C. O'Brien, and A. Suzuki, eds., Springer, Cham, 2020, pp. 341–51.
33. T. Murakumo, Y. Koizumi, K. Kobayashi, H. Harada, Creep strength of Ni-base single-crystal superalloys on the γ/γ' tie-line, in: Superalloys 2004, 2004: pp. 155–62. https://doi.org/10.7449/2004/Superalloys_2004_155_162.
34. A.F. Giamei and D.L. Anton: *Metall. Trans. A*, 1985, vol. 16, pp. 1997–2005. https://doi.org/10.1007/BF02662400.
35. X. Wu, S.K. Makineni, C.H. Liebscher, G. Dehm, J. Rezaei Mianroodi, P. Shanthraj, B. Svendsen, D. Bürger, G. Eggeler, D. Raabe, and B. Gault: *Nat. Commun.*, 2020, vol. 11, p. 389. https://doi.org/10.1038/s41467-019-14062-9.
36. R. Darolia, D.F. Lahrman, R.D. Field, and R. Sisson: *Superalloys*, 1988, vol. 1988, pp. 255–64.
37. C.M.F. Rae and R.C. Reed: *Acta Mater.*, 2001, vol. 49, pp. 4113–25.
38. R. Rettig and R.F. Singer: *Acta Mater.*, 2011, vol. 59, pp. 317–27.
39. M. Pessah, P. Caron, T. Khan, Effect of μ Phase on the Mechanical Properties of a Nickel-Base Single Crystal Superalloy, in: S.D. Antolovich, R.W. Stusrud, R.A. MacKay, D.L. Anton, T. Khan, R.D. Kissinger, D.L. Klarstrom (Eds.), Superalloys 1992, TMS, 1992: pp. 567–76.
40. Kevin S. O'Hara, William S. Walston, Earl W. Ross, Ramgopal Darolia, Nickel base superalloy and article, US5482789A, 1996.
41. J.X. Zhang, T. Murakumo, Y. Koizumi, T. Kobayashi, H. Harada, and S. Masaki Jr.: *Metall. Mater. Trans. A*, 2002, vol. 33A, pp. 3741–46.
42. S. Walston, A. Cetel, R. MacKay, K. O'Hara, D. Duhl, R. Dreshfield, Joint development of a fourth generation single crystal superalloy, in: Proc. Int. Symp. Superalloys, 2004: pp. 15–24. http://www.scopus.com/inward/record.url?eid=2-s2.0-23744513914&partnerID=tZOtx3y1.
43. A.C. Yeh and S. Tin: *Metall. Mater. Trans. A*, 2006, vol. 37A, pp. 2621–31. https://doi.org/10.1007/BF02586097.
44. A. Sato, H. Harada, A.-C. Yeh, K. Kawagishi, T. Kobayashi, Y. Koizumi, T. Yokokawa, J.X. Zhang, A 5th generation SC superalloy with balanced high temperature properties and processability, in: Superalloys 2008, 2008: pp. 131–38. https://doi.org/10.7449/2008/Superalloys_2008_131_138.
45. K. Kawagishi, A. Sato, H. Harada, A.-C. Yeh, Y. Koizumi, and T. Kobayashi: *Mater. Sci. Technol.*, 2009, vol. 25, pp. 271–75. https://doi.org/10.1179/174328408X361517.
46. T. Saito, H. Harada, T. Yokokawa, M. Osawa, K. Kawagishi, and S. Suzuki: *Mater. Trans.*, 2024, vol. 65, pp. 1443–57. https://doi.org/10.2320/matertrans.MT-M2024081.

47. R.A. MacKay, L.J. Ebert, The development of γ-γ' lamellar structures in a nickel-base superalloy during elevated temperature mechanical testing, Metall. Trans. A 16 (1985). https://doi.org/10.1007/BF02662398.
48. N. Matan, D.C. Cox, C.M.F. Rae, and R.C. Reed: On the kinetics of rafting in CMSX-4 superalloy single crystals. *Acta Mater*., 1999, vol. 47, pp. 2031–45. https://doi.org/10.1016/S1359-6454(99)00093-2.
49. F.R.N. Nabarro, C.M. Cress, and P. Kotschy: *Acta Mater*., 1996, vol. 44, pp. 3189–98. https://doi.org/10.1016/1359-6454(95)00423-8.
50. Y. Koizumi, T. Kobayashi, T. Yokokawa, J. Zhang, M. Osawa, H. Harada, Y. Aoki, M. Arai, Development of next-generation Ni-base single crystal superalloys, in: Proc. Int. Symp. Superalloys, 2004: pp. 35–43. https://doi.org/10.7449/2004/Superalloys_2004_35_43.
51. J. Zhang, J. Wang, H. Harada, and Y. Koizumi: *Acta Mater*., 2005, vol. 53, pp. 4623–33. https://doi.org/10.1016/j.actamat.2005.06.013.
52. Y. Li, L. Wang, Y. He, W. Zheng, L. Lou, and J. Zhang: *Scr. Mater*., 2022, vol. 217, 114769https://doi.org/10.1016/j.scriptamat.2022.114769.
53. L.J. Carroll, Q. Feng, and T.M. Pollock: *Metall. Mater. Trans. A*, 2008, vol. 39A, pp. 1290–1307. https://doi.org/10.1007/s11661-008-9520-7.
54. R.C. Reed, N. Matan, D.C. Cox, M.A. Rist, and C.M.F. Rae: *Acta Mater*., 1999, vol. 47, pp. 3367–81. https://doi.org/10.1016/S1359-6454(99)00217-7.
55. Q. Yue, L. Liu, W. Yang, T. Huang, J. Zhang, and H. Fu: *Mater. Sci. Eng. A*, 2019, vol. 742, pp. 132–37. https://doi.org/10.1016/j.msea.2018.10.063.
56. Y. Koizumi, K. Kawagishi, T. Yokokawa, M. Yuyama, Y. Takata, and H. Harada: Hot corrosion and creep properties of Ni-base single-crystal superalloys, in *Superalloys 2020*. S. Tin, M. Hardy, J. Clews, J. Cormier, Q. Feng, J. Marcin, C. Orien, and A. Suzuki, eds., Springer, Cham, 2020, pp. 747–52.
57. T. Yokokawa, H. Harada, Y. Mori, K. Kawagishi, Y. Koizumi, T. Kobayashi, M. Yuyama, S. Suzuki, Design of Next Generation Ni-base Single Crystal Superalloys Containing Ir: Towards 1150 °C Temperature Capability, in: Superalloys 2016, 2016: pp. 123–30. https://doi.org/10.1002/9781119075646.ch14.
58. Y. Cheng, X. Zhao, W. Xia, Q. Pan, Q. Yue, Y. Gu, and Z. Zhang: *Prog. Nat. Sci. Mater. Int*., 2022, vol. 32, pp. 745–51. https://doi.org/10.1016/j.pnsc.2022.10.001.
59. R.A. MacKay, M.V. Nathal, and D.D. Pearson: *Metall Trans. Phys. Metall. Mater. Sci*., 1990, vol. 21A(1), pp. 381–88.
60. Y. Mori, T. Yokokawa, T. Kobayashi, H. Harada, and S. Suzuki: *Mater. Trans*., 2016, vol. 57, pp. 1845–48. https://doi.org/10.2320/matertrans.MAW201606.
61. H. Harada, M. Yamazaki, Y. Koizumi, N. Sakuma, N. Furuya, H. Kamiya, Alloy design for nickel-base superalloys BT—high temperature alloys for gas turbines 1982. In: R. Brunetaud, D. Coutsouradis, T.B. Gibbons, Y. Lindblom, D.B. Meadowcroft, R. Stickler (Eds.), Springer, Dordrecht, 1982: pp. 721–35.
62. T. Yokokawa, H. Harada, K. Kawagishi, T. Kobayashi, M. Yuyama, Y. Takata, Advanced Alloy Design Program and Improvement of Sixth-Generation Ni-Base Single Crystal Superalloy TMS-238, in: S. Tin, M. Hardy, J. Clews, J. Cormier, Q. Feng, J. Marcin, C. O'Brien, A. Suzuki (Eds.), Superalloys 2020, Springer International Publishing, Cham, 2020: pp. 122–30. https://doi.org/10.1007/978-3-030-51834-9_12.
63. A. Sato, H. Harada, T. Yokokawa, T. Murakumo, Y. Koizumi, T. Kobayashi, and H. Imai: *Scr. Mater*., 2006, vol. 54, pp. 1679–84. https://doi.org/10.1016/j.scriptamat.2006.01.003.
64. S. Utada, Y. Joh, M. Osawa, T. Yokokawa, T. Sugiyama, T. Kobayashi, K. Kawagishi, S. Suzuki, and H. Harada: *Metall. Mater. Trans. A*, 2018, vol. 49A, pp. 4029–41. https://doi.org/10.1007/s11661-018-4710-4.
65. T. Yokokawa, M. Osawa, K. Nishida, T. Kobayashi, Y. Koizumi, and H. Harada: *Scr. Mater*., 2003, vol. 49, pp. 1041–46. https://doi.org/10.1016/S1359-6462(03)00437-8.
66. S.K. Makineni, M. Lenz, S. Neumeier, E. Spiecker, D. Raabe, and B. Gault: *Scr. Mater*., 2018, vol. 157, pp. 62–66. https://doi.org/10.1016/j.scriptamat.2018.07.042.
67. I. Gutierrez-Urrutia, S. Zaefferer, and D. Raabe: *JOM*, 2013, vol. 65, pp. 1229–36. https://doi.org/10.1007/s11837-013-0678-0.
68. T. Saito, M. Yuyama, and H. Murakami: *J. Alloys Compd*., 2025, vol. 1022, 179871. https://doi.org/10.1016/j.jallcom.2025.179871.
69. K. Harris, G.L. Erickson, W.D. Brentnall, J.M. Aurrecoechea, S.L. Sikkenga, and K.G. Kubarych: Development of the Rhenium Containing Superalloys CMSX-4 & CM 186 LC for Single Crystal Blade and Directionally Solidified Vane Applications in Advanced Turbine Engines, in *Superalloys 1992*. S.D. Antolovich, R.W. Stusrud, R.A. MacKay, D.L. Anton, T. Khan, R.D. Kissinger, and D.L. Klarstrom, eds., Springer, Amsterdam, 1992, pp. 297–306.
70. J. Schindelin, I. Arganda-Carreras, E. Frise, V. Kaynig, M. Longair, T. Pietzsch, S. Preibisch, C. Rueden, S. Saalfeld, B. Schmid, J.-Y. Tinevez, D.J. White, V. Hartenstein, K. Eliceiri, P. Tomancak, and A. Cardona: *Nat. Methods*, 2012, vol. 9, pp. 676–82. https://doi.org/10.1038/nmeth.2019.
71. I. Arganda-Carreras, V. Kaynig, C. Rueden, K.W. Eliceiri, J. Schindelin, A. Cardona, and H. Sebastian Seung: *Bioinformatics*, 2017, vol. 33, pp. 2424–26. https://doi.org/10.1093/bioinformatics/btx180.
72. Simon Klein, Plugin for ImageJ to measure linear distances for binary images in X and Y Direction, (2016). https://github.com/kleinsimon/LinearDistance/.
73. Y. Joh, S. Utada, M. Osawa, T. Kobayashi, T. Yokokawa, K. Kawagishi, S. Suzuki, and H. Harada: *Mater. Trans*., 2016, vol. 57, pp. 1305–08. https://doi.org/10.2320/matertrans.M2016032.
74. Y. Mori, T. Yokokawa, T. Kobayashi, H. Harada, S. Suzuki, Y. Takebe, Microstructure and Creep Strength of the Ni-Base Single Crystal Superalloys Containing Ir Substituting for Ru, in: *Proc. 9th Pac. Rim Int. Conf. Adv. Mater. Process. PRICM9*, The Japan Institute of Metals and Materials, n.d.: pp. 765–69.
75. H. Murakami, T. Honma, Y. Koizumi, H. Harada, Distribution of Platinum Group Metals in Ni-Base Single-Crystal Superalloys, in: Superalloys 2000 Ninth Int. Symp., TMS, 2000: pp. 747–56. https://doi.org/10.7449/2000/Superalloys_2000_747_756.
76. A.P. Ofori, C.J. Humpherys, S. Tin, C.N. Jones, A TEM Study of the Effect of Platinum Group Metals in Advanced Single Crystal Nickel-Base Superalloys, in: *Superalloys 2004 Tenth Int. Symp*., TMS, 2004: pp. 787–94. https://doi.org/10.7449/2004/Superalloys_2004_787_794.
77. J.S. Van Sluytman, A.L. Fontaine, J.M. Cairney, and T.M. Pollock: *Acta Mater*., 2010, vol. 58, pp. 1952–62. https://doi.org/10.1016/j.actamat.2009.11.038.
78. S. Neumeier, F. Pyczak, and M. Göken: *Mater. Des*., 2021, vol. 198, 109362. https://doi.org/10.1016/j.matdes.2020.109362.
79. Y. Takebe, T. Yokokawa, T. Kobayashi, K. Kawagishi, H. Harada, and C. Masuda: *J. Jpn. Inst. Met*., 2015, vol. 79, pp. 227–31. https://doi.org/10.2320/jinstmet.JBW201402.
80. R.A. MacKay, L.J. Ebert, Factors Which Influence Directional Coarsening of γ' During Creep in Nickel-Base Superalloy Single Crystals, in: *Superalloys 1984 Fifth Int. Symp*., TMS, 1984: pp. 135–44. https://doi.org/10.7449/1984/Superalloys_1984_135_144.
81. T. Hino, T. Kobayashi, H. Harada, T. Yamagata, Development of a New Single Crystal Superalloy for Industrial Gas Turbines, in: *Superalloys 2000 Ninth Int. Symp*., TMS, 2000: pp. 729–36. https://doi.org/10.7449/2000/Superalloys_2000_729_736.
82. I. Steinbach, I. Roslyakova, K. Abrahams, Fundamentals: alloy thermodynamics and kinetics of diffusion, in: Nickel Base Single Cryst. Length Scales, Elsevier, Amsterdam, 2022: pp. 21–40. https://doi.org/10.1016/B978-0-12-819357-0.00009-3.
83. C. Schulze and M. Feller-Kniepmeier: *Mater. Sci. Eng. A*, 2000, vol. 281, pp. 204–12. https://doi.org/10.1016/S0921-5093(99)00713-3.
84. A. Lasalmonie and J.L. Strudel: *Philos. Mag. J. Theor. Exp. Appl. Phys*., 1975, vol. 32, pp. 937–49. https://doi.org/10.1080/14786437508221665.
85. Q. Shi, J. Huo, Y. Zheng, and Q. Feng: *Mater. Sci. Eng. A*, 2018, vol. 725, pp. 148–59. https://doi.org/10.1016/j.msea.2018.04.026.
86. S. Ma, L. Carroll, and T.M. Pollock: *Acta Mater*., 2007, vol. 55, pp. 5802–12. https://doi.org/10.1016/j.actamat.2007.06.042.
87. Z. Zhong, H. Wang, S. Zhang, G. Li, H. Duan, C. Fan, H. Zhang, C. Ai, Y. Ru, Y. Pei, S. Li, and S. Gong: *J. Mater. Res. Technol*., 2025, vol. 39, pp. 2742–51. https://doi.org/10.1016/j.jmrt.2025.09.273.

88. A. Bezold, H.J. Stone, C.M.F. Rae, and S. Neumeier: *Metall. Mater. Trans. A*, 2022, vol. 53A, pp. 2890–2901. https://doi.org/10.1007/s11661-022-06713-2.
89. X. Yao, Q. Ding, X. Zhao, X. Wei, J. Wang, Z. Zhang, and H. Bei: *Mater. Today Nano*, 2022, vol. 17, 100152. https://doi.org/10.1016/j.mtnano.2021.100152.
90. S. Utada, M. Heczko, J. Rame, S. Hamadi, A. Dlouhý, T. Kruml, P. Villechaise, R.C. Reed, M.J. Mills, and J. Cormier: *Acta Mater.*, 2025, vol. 299, 121448. https://doi.org/10.1016/j.actamat.2025.121448.
91. S. Gao, Y. Zhou, C.-F. Li, Z.-Q. Liu, and T. Jin: *J. Alloys Compd.*, 2016, vol. 671, pp. 458–64. https://doi.org/10.1016/j.jallcom.2016.02.122.
92. M.S.A. Karunaratne and R.C. Reed: *Acta Mater.*, 2003, vol. 51, pp. 2905–19. https://doi.org/10.1016/S1359-6454(03)00105-8.
93. J. Chen, L. Zhang, and X.-G. Lu: *Metall. Mater. Trans. A*, 2018, vol. 49A, pp. 2999–3010. https://doi.org/10.1007/s11661-018-4669-1.
94. A. Cervellon, S. Hémery, P. Kürnsteiner, B. Gault, P. Kontis, and J. Cormier: *Acta Mater.*, 2020, vol. 188, pp. 131–44. https://doi.org/10.1016/j.actamat.2020.02.012.
95. P. Kontis and T.M. Smith: *Metall. Mater. Trans. A*, 2024, vol. 55A, pp. 4723–41. https://doi.org/10.1007/s11661-024-07626-y.
96. N. Karpstein, M. Wu, A. Bezold, S. Neumeier, J. Cormier, and E. Spiecker: Temperature and time dependence of elemental segregation at stacking faults in Ni- and Co-base superalloys, in *Superalloys 2024*. J. Cormier, I. Edmonds, S. Forsik, P. Kontis, C. O'Connell, T. Smith, A. Suzuki, S. Tin, and J. Zhang, eds., Springer, Cham, 2024, pp. 502–11.
97. Y. Cheng, X. Zhao, W. Xia, J. Xu, Q. Yue, J. Wang, Y. Yuan, W. Yang, Y. Gu, and Z. Zhang: *Mater. Today Nano*, 2025, vol. 32, 100694. https://doi.org/10.1016/j.mtnano.2025.100694.
98. T. Kobayashi, H. Harada, M. Osawa, and A. Sato: *J. Jpn. Inst. Met.*, 2005, vol. 69, pp. 1099–1103. https://doi.org/10.2320/jinstmet.69.1099.
99. Furuya Meta Co, Ltd., FMBI Price, (n.d.). https://furuyametal.jp/english/fmbi/chart/?language=en. Accessed 30 Sept 2025.
100. J.S. Van Sluytman, A. Suzuki, A. Bolcavage, R.C. Helmink, D.L. Ballard, T.M. Pollock, Gamma Prime Morphology and Creep Properties of Nickel Base Superalloys with Platinum Group Metal Additions, in: Superalloys 2008 Elev. Int. Symp., TMS, 2008: pp. 499–508. https://doi.org/10.7449/2008/Superalloys_2008_499_508.
101. Toshiharu Kobayashi, Yutaka Koizumi, Hideyuki Murakami, Yoshikazu Ro, Yoko Yamabe, Shizuo Nakazawa, Hiroshi Harada, Toshihiro Yamagata, Iridium-containing nickel-base superalloy, US6494971B1, 2002. https://patents.google.com/patent/US6494971B1/en.